Alaskan-type Kedanshan intrusive complex, central Inner Mongolia, China: Superimposed subduction between the Mongol-Okhotsk and Paleo-Pacific oceans in the Jurassic

Jinlong Dong [a], Shuguang Song [a*], Mingming Wang [a], Mark B. Allen [b], Li Su[c], Chao Wang [a], Liming Yang [a], Bei Xu [a]

[a] *MOE Key Laboratory of Orogenic Belts and Crustal Evolution, School of Earth and Space Science, Peking University, Beijing, China*

[b] *Department of Earth Sciences, University of Durham, Durham, UK*

[c] *Institute of Geology and Geophysics, Chinese Academy of Science, Beijing, China*

[*] Corresponding author: Shuguang Song

Email: sgsong@pku.edu.cn

MS for *Journal of Asian Earth Sciences* (special issue for Prof. Jahn Part 2)

Abstract

The Xing'an-Inner Mongolia accretionary belt in the eastern Central Asian Orogenic Belt (CAOB) was produced by the subduction of three oceanic plates: the Paleo-Asian, Mongol-Okhotsk and Paleo-Pacific oceans. The interactions between these plates remain unclear. Here we report an Alaskan-type ultramafic-mafic intrusive complex in the Kedanshan area, central Inner Mongolia, China. The main lithologies of this intrusive complex include cumulate dunite, pyroxene peridotite, olivine pyroxenite and cumulate gabbro, with late gabbroic/anorthositic veins. Minerals and whole-rock compositional variations display characteristics of an arc cumulate trend (Alaskan-type), through fractional crystallization of Mg-rich and hydrous basaltic magma associated with oceanic subduction. Zircons from gabbro samples yield long-loved Jurassic ages of ~193±6 Ma to 179±4 Ma. We conclude that this ultramafic-mafic complex is an accumulated intrusion from an arc-related, high-Mg magma chamber in the metasomatized mantle wedge above a subduction zone. Considering the ages, location and tectonic setting of the complex, we suggest that it was most likely generated by melting of a large and triangle-shaped mantle wedge during superimposed subduction between the Mongol-Okhotsk Ocean and the Paleo-Pacific Ocean in the Jurassic.

Keywords: Alaskan-type ultramafic-mafic intrusion; Jurassic; Superimposed subduction; Mongol-Okhotsk Ocean; Paleo-Pacific Ocean

1. Introduction

Ultramafic-mafic rock complexes provide keys to understanding the mantle

compositions, deep geodynamic processes and the tectonic setting of their host intrusions (e.g., KePezhinskas et al., 1997; Meibom et al., 2002; Polat et al., 2011). Many ultramafic-mafic rocks, including mantle peridotites and cumulates in the lower part of ophiolites, are commonly associated with mineral resources such as Fe, V, Ni, Cu and the platinum group elements (PGE). Alaskan-type complexes are characterized by a concentric layout of rock types, e.g., a cumulate dunite core surrounded by wehrlite, olivine clinopyroxenite, clinopyroxenite, magnetite -hornblende clinopyroxenite, hornblendite and gabbro. Such complexes are considered to be the mark of island arc or active continental margin settings (Murray, 1972; Tistl et al, 1994; Helmy and EI Mahallawi, 2003; Thakurta et al., 2008; Zhang., 2014) and closely related to PGE mineralization (Irvine, 1974; Ishiwatari and Ichiyama, 2004; Thakurta et al., 2008; Ripley, 2009; Su et al., 2013). Therefore, understanding of the petrogenesis, tectonic environment and source characteristics of ultramafic-mafic rocks is significant for reconstructing the regional geological evolution.

Central Inner Mongolia is located in the southeastern segment of the Central Asian Orogenic Belt (CAOB). In this region, three tectonic domains join together, including the Paleo-Asian Ocean tectonic domain itself, and the Mongol-Okhotsk Ocean in the north and Paleo-Pacific Ocean tectonic domain in the east (e.g., Zonenshain et al., 1990; Zorin, 1999; Sorokin et al., 2004; Wu et al., 2011; Xu et al., 2013a; Xu et al., 2013b, 2015; Wang et al., 2011, 2012, 2015a). The CAOB was produced by the long-lived subduction and eventual closure of the Paleo-Asian Ocean and by the convergence between the

North China Craton and the Mongolian micro-continent (e.g., Xiao et al., 2003, 2009; Song et al., 2015). The Mongol-Okhotsk Ocean was a large embayment of the Paleo-Pacific Ocean (Zonenshain et al., 1990; Zorin et al., 1999; Donskaya et al., 2013), and it played a significant role in the tectonic evolution of the eastern part of Eurasia since the Mesozoic (e.g., Xu et al., 2013a; Tang et al., 2014). The Paleo-Pacific Oceanic domain was produced by the westward subduction of the Izanagi Plate, which controlled the evolution of the East Asian continental margin since the Mesozoic (e.g., Guo et al., 2007; Wu et al., 2011). Ultramafic-mafic blocks crop out in central Inner Mongolia, and most of them have been shown to be the basal part of the Paleozoic ophiolitic sequences. Based on ages of the ophiolite suites, most researchers suggested that the closure time of the Paleo-Asian Ocean was in the Late Permian or Early Triassic (e.g., Xiao et al., 2003, 2009; Li et al., 2012a; Jian et al., 2012; Cheng et al., 2014; Song et al., 2015; Guo et al., 2016). However, Late Mesozoic ultramafic-mafic outcrops in central Inner Mongolia are sparsely documented. In general, Early Jurassic (204-180 Ma) magmatic records are scarce in this region (Tong et al., 2010; Wang et al., 2015a).

The Kedanshan ultramafic-mafic intrusion has long been regarded as a component of ophiolite associated with the Paleo-Asian Ocean. In this paper, we present a comprehensive study, including petrologic, mineralogical, geochemical and chronological data, for this intrusion. We confirm that it is an Alaskan-type complex that formed in the Jurassic (193-179 Ma). These data provide evidence for superimposed subduction between the Mongol-Okhotsk Ocean and the Paleo-Pacific Ocean in the Jurassic.

2. Geological background

The Kedanshan ultramafic-mafic intrusion is located ~80 km southwest of Linxi in central Inner Mongolia (Fig. 1). Tectonically, it is located within the Solonker-Linxi SSZ ophiolite belt of the Xing'an-Inner Mongolia accretionary belt (XIMAB) of the CAOB. To the north is the Mongol-Okhotsk orogenic belt (Fig.1A) and to the east is the western part of the Paleo-Pacific subduction zone (Fig.1A). The Mongol-Okhotsk orogenic belt is located between northern Mongolia and Siberia Craton and extends over 3000 km in a northeast-southwest orientation (Fig. 1A). The closure of the Mongol-Okhotsk Ocean was suggested to have occurred in a scissor-like style that started in the Triassic-Late Jurassic (Zonenshain et al., 1990) or Early Middle Jurassic (Zorin, 1999) from the west, and finished in the Late Jurassic-Early Cretaceous to the east (Cogné et al., 2005). The Paleo-Pacific tectonic domain is associated with westward subduction of the Paleo-Pacific Ocean in the Early Mesozoic (Wu et al., 2007; Zhou and Wilde, 2013; Zhou et al., 2014; Wang et al., 2015a; Niu et al., 2015). The XIMAB comprises a series of suture zones, arcs, micro-continental blocks and orogenic belts between the North China Craton and the Mongolia micro-continent, and occurred chiefly during the Paleozoic (Fig.1B, Xiao et al., 2003, 2009; Miao et al., 2007, 2008; Jian et al., 2012; Xu et al., 2013b, 2015; Zhao et al., 2014; Song et al., 2015).

The studied region consists of Ordovician (Baoerhantu Group) and Late Jurassic sedimentary-volcanic strata (Manketouebo Group), and intrusive rocks including the Kedanshan ultramafic-mafic complex and a Late Jurassic monzonite granite (Fig.1C).

The Ordovician strata (Baoerhantu Group) consist mainly of metamorphic sandstone and siliceous rock and occupy an area of less than 40 km^2. The Late Jurassic sedimentary-volcanic strata consist of rhyolitic ignimbrite, rhyolitic volcanic breccia, rhyolite, reworked tuff and tuffaceous sandstone.

3. Petrography

The Kedanshan ultramafic-mafic intrusion is ~1.7 km long and ~1.2 km wide and occupies an area of ~1.4 km^2. Except for off-white gabbro and anorthosite, most rocks in the Kedanshan ultramafic-mafic intrusion are dark colored, showing weak striped texture and strong serpentinization, which makes it difficult to distinguish lithologies in the field (Fig. 2). The off-white gabbro/anorthosite occurs either as veins (Fig. 2A and C) or as interlayers with peridotite (Fig. 2B). The layered gabbro shows an obvious cumulate structure in the field (Fig. 2D). According to the mineral assemblage and modal contents, five distinct lithologic types can be recognized (Fig. 3): (1) dunite, (2) pyroxene peridotite, (3) olivine pyroxenite, (4) pyroxenite and gabbro, and (5) gabbro/anorthosite veins.

3.1 Dunite

Olivine grains in dunite are totally serpentinized. Some dunite samples contain nearly 100 vol.% olivine with ~2 vol.% chromian spinel, and others have small amount of clinopyroxene (<10 vol.%). They show medium- to coarse-grained inequigranular to granoblastic textures without deformation (Fig. 3A to C). The serpentinized olivine is oval-shaped, subhedral crystals with size ranging from 0.5 to 1.5 mm, and displays

typical cumulate texture with orientated long-axes. Clinopyroxene grains (0.1 to 0.5 mm) occur as intercumulus grains between olivines (Fig. 3B and C). Chromian spinel consists of disseminated euhedral to subhedral crystals between and within other minerals (Fig. 3A to C).

3.2 Peridotite

The peridotite consists of olivine (~40-70 vol.%), clinopyroxene (~30-50 vol.%), orthopyroxene (~5-10 vol.%) and chrome spinel (~3-4 vol.%), showing a massive micro- to fine-grained granoblastic texture (Fig. 3D). Olivine grains in peridotite were partly serpentinized (Fig. 3D) along cracks or grain boundaries (Fig. 3D). Clinopyroxene occurs as either dispersed grains or intercumulus between olivine crystals (Fig. 3D). Disseminated chromian spinels (~0.05 to 0.2 mm) occur as euhedral to subhedral grains, and they are partially or totally included in silicate minerals indicating their early crystallization.

3.3 Olivine pyroxenite

The olivine pyroxenite consists mainly of 70-80 vol.% clinopyroxene and 5-30 vol.% olivine with less than 10 vol.% orthopyroxene and opaque minerals (Fig. 3E and F). It shows medium-grained inequigranular or granoblastic textures (Fig. 3E and F). Clinopyroxene grains are subhedral to euhedral and vary in size (0.1 to 1.5 mm) (Fig. 3E and F). Olivine forms euhedral crystals (0.1 to 0.4 mm) and occurs intercumulus between pyroxene grains (Fig. 3E and F).

3.4 Pyroxenite and gabbro

Lithologies of the layered gabbro vary from Pl-poor pyroxenite to Pl-rich gabbro with the modal change of 15-70 vol.% plagioclase, 10-55 vol.% clinopyroxene, 2-8 vol.% orthopyroxene with minor sulfide (Fig. 3G to I). They have medium- to fine-grained textures, and display characteristic cumulate features with abundant clinopyroxene and plagioclase (Fig. 3G to I). Orthopyroxene occurs as subhedral, crystals in concordance with Cpx (Fig. 3G). Plagioclase crystals are strongly altered (Fig. 3G to I); they occur as either interstitial phases between pyroxene grains, or enclose clinopyroxene crystals, indicating their late crystallization (Fig. 3G to I).

4. Analytical methods

4.1 Mineral chemistry

Mineral analyses were done on a JEOL JXA-8100 Electron Probe Microanalyzer (EPMA) at Peking University. Analytical conditions were optimized for standard silicates and oxides at 15 kV accelerating voltage with a 20 nA focused beam current for all the elements. Routine analyses were obtained by counting for 30 seconds at peak and 10 seconds on background. Repeated analysis of natural and synthetic mineral standards yielded precisions better than ± 2% for most elements.

4.2 Whole-rock major and trace element analyses

Based on careful petrographic observation, we selected thirteen samples for using whole rock major and trace element analyses. These representative samples include dunite, pyroxene peridotite, olivine pyroxenite, and gabbro. Whole-rock major element

oxides (SiO_2, TiO_2, Al_2O_3, FeO, MnO, MgO, CaO, Na_2O, K_2O, and P_2O_5) were determined using inductively coupled plasma-optical emission spectroscopy (ICP-OES) at China University of Geosciences, Beijing (CUGB). The analytical precisions (1σ) for most major elements based on rock standards AGV-2 (US Geological Survey), GSR-1, GSR-3 and GSR-5 (National geological standard reference materials of China) are better than 1% with the exception of TiO_2 (~1.5%) and P_2O_5 (~2.0%). Loss on ignition (LOI) was determined by placing 1 g of samples in the furnace at 1000 °C for several hours before being cooled in a desiccator and reweighed (Song et al., 2010).

The trace element analysis for Kedanshan ultramafic-mafic samples was performed on an Agilent-7500a inductively coupled plasma mass spectrometer (ICP-MS) in the Institute of Earth Science of CUGB. About 40 mg of sample powder was dissolved in equal mixture of subboiling distilled HNO_3 and HF with a Teflon digesting vessel on a hotplate at 185 °C for 48 h using high-pressure bombs for digestion/dissolution. The samples were then evaporated to incipient dryness, refluxed with 6 N HNO_3, and heated again to incipient dryness. The sample was again dissolved in 2 mL of 3 N HNO_3 in high-pressure bombs for a further 24 h to ensure complete dissolution. Such digested samples were diluted with Milli-Q water to a final dilution factor of 2000 in 2% HNO_3 solution with total dissolved solid of 0.05 %. Precisions (1σ) for most elements based on liquid standards Std-1, Std-2, Std-4 (AccuStandard, USA). Rock standards AGV-2 (US Geological Survey), and GSR-1, GSR-3, GSR-5 (National geological standard reference materials of China) were used to monitor the analytical accuracy and precision. The

analytical accuracy, as indicated by relative difference between measured and recommended values, is better than 5% for most elements, and 10-15% for Cu, Zn, Gd and Ta.

4.3 Zircon U-Pb geochronology

Zircons were separated from three gabbroic samples (13LX-17, 13LX-18 and 13LX-19) by using standard density and magnetic separation techniques and selected by handpicking under a binocular microscope. The Cathodoluminescence (CL) examination was done by using an FEI QUANTA650 FEG Scanning Electron Microscope (SEM) under conditions of 15 kV/120 nA in the School of Earth and Space Sciences, Peking University, Beijing.

Measurements of U, Th and Pb in zircons were carried out on an Agilent-7500a quadrupole inductively coupled plasma mass spectrometry coupled with a New Wave SS UP193 laser sampler (LA-ICP-MS) at CUGB. Laser spot size of 36 μm, laser energy density of 8.5 J/cm^2 and a repetition rate of 10 Hz were applied for analysis (see Song et al., 2010 for more details). Age calculations and plots of concordia diagrams were done using Isoplot (Ludwig, 2003).

5 Results

5.1 Mineral chemistry

5.1.1 Olivine

Because the olivine in all the dunite samples has been altered into serpentine (Fig. 3A to C), we cannot see the complete variation of olivine compositions from dunite to

pyroxenite. Olivine in pyroxene-peridotite and olivine-bearing pyroxenite shows a narrow compositional change of forsterite contents (Fo) from 85.3 to 83.4, with NiO contents vary from 0.03 to 0.23 wt.% (Table S1; Fig. 4A). The olivines are also characterized by extremely low CaO contents (< 0.14 wt.%), similar to olivines from the Alaksan type complexes, much lower than olivines from komatiite and picrite (Fig. 4B).

5.1.2 Pyroxene

Representative pyroxene compositions of the studied samples are given in Table S2 and shown in a ternary plot of the Wo-En-Fs diagram (Fig. 5A). The clinopyroxenes are mostly diopsides with subordinate augites, and are Ca-rich with a formula of $Wo_{39.2-48.8}En_{42.9-52.5}Fs_{4.2-13.7}$. Their Mg# [100×Mg/(Mg + Fe^{2+})] varies from 92.1 in the dunite to 75.7 in gabbro, and is positively correlated with Cr_2O_3 (Fig. 5B, Table S2). All clinopyroxenes in the studied samples are characterized by low TiO_2 (0-0.53 wt.%), Cr_2O_3(0.04-1.00 wt.%), Al_2O_3 (1.11-6.89 wt.%) and Na_2O (0-0.87 wt.%), showing a narrow compositional range (Table S2). In the Alz versus TiO_2 wt.% diagram (Fig. 5C), clinopyroxene compositions plot in the Alaskan-type field and show an arc cumulate trend. The homogeneous TiO_2 and Al_2O_3, as well as high CaO, are similar to those from Alaskan-type intrusions in many places worldwide (Snoke et al. 1981; Helmy and EI Mahallawi, 2003; Farahat and Helmy, 2006; Helmy et al., 2015).

Orthopyroxene (Opx) is rare in the Kedanshan ultramafic-mafic intrusion, and its composition is bronzite with a formula of $Wo_{1.4-1.7}En_{73.9-83.7}Fs_{14.8-24.4}$ (Fig. 5A).

5.1.3 Plagioclase

Representative plagioclase compositions are given in Table S3. Plagioclases in layered gabbro have homogeneous compositions without chemical zonation. They are Ca-rich (18.59-20.56 wt.%) with anorthite (An) contents from 91.39 to 98.04 wt.%, consistent with An contents from Alaskan-type complexes (e.g., Irvine, 1974; Himmelberg and Lonely, 1995).

5.1.4 Chromian spinel

Chromian spinel occurs as an accessory mineral in dunite and pyroxene peridotite. Representative analytical data of chromian spinels from these rocks are shown in Table S4. They are characterized by low content of TiO_2, varying contents of Cr_2O_3, FeO_T and MgO, and a negative correlation between Cr_2O_3 and MgO contents. Cr# [100×Cr/(Cr+Al)] values of chromian spinels systematically change from 69.2-40.9 (average, 52.1) in dunite, 55.8-43.5 in pyroxene peridotite, to 39.0 in olivine pyroxenite. As shown in Fig. 6, all these chromian spinels have chemical features similar to those from Alaskan-type complexes (Snoke et al., 1981; Himmelberg and Loney, 1995; Helmy et al., 2015), but are distinguishable from spinels from ophiolites, MORB, boninites and abyssal peridotites.

5.2 Whole-rock geochemistry

The major and trace element compositions for representative samples from the Kedanshan ultramafic-mafic intrusion are listed in Table 1. These samples show wide compositional variation in both major and trace elements from dunite, pyroxene

peridotite, olivine pyroxenite to gabbro. MgO contents are positively correlated with TiO_2 and Yb in gabbros, but negatively correlated with TiO_2 and Yb in dunites and peridotites (Fig. 7A and B). All rocks show negative correlations in MgO vs. Al_2O_3 and CaO (Fig. 7C and D), but have different trends in MgO vs. CaO/Al_2O_3 in peridotites and gabbros (Fig. 7E). The compatible elements (Co, Cr and Ni) are positively correlated with MgO contents (Fig. 7F-H). The positive correlation between Cr and Ni contents (Fig. 7I) suggests that fractional evolution of magma is firstly controlled by olivine and then by clinopyroxene. The systematic variations of compositions from dunite to gabbro (Fig. 7A-H) indicate that the Kedanshan ultramafic-mafic intrusion originated from various degrees of fractional crystallization from an identical magma type (see below).

The chondrite-normalized REE and primitive mantle-normalized multi-element diagrams are shown in Fig. 8. The total of REEs of the studied samples varies from 0.31 ppm in dunite to 5.71 ppm in gabbro. They exhibit significant variation in normalized element patterns (Fig. 8A). The dunite and peridotite samples display LREE enriched (U-shaped) patterns with various extent of negative Eu anomaly (Eu/Eu^*=0.20-0.99), while the olivine pyroxenite and gabbro exhibit LREE depleted patterns (LREE/HREE=0.73-1.17), with a strongly positive Eu anomaly in gabbroic samples (Eu/Eu^*=1.30-1.75). In primitive mantle-normalized multi-element diagrams (Fig. 8B), the studied samples display arc-like patterns characterized by enrichments in LILEs relative to HFSEs (Gill, 1981; Grove et al., 2003), and have positive anomalies in Ba, U, Pb and Sr, and various Nb and Ta anomalies. Significant variations of trace elements

from dunite to gabbro indicate an obvious process of fractional crystallization. The positive Eu, Ba and Sr anomalies from gabbro are originated from plagioclase accumulation (Niu and O'Hara, 2009). The various negative Eu anomalies in ultramafic rocks indicate the absence of plagioclase in the process of their crystallization, which is supported by their petrography.

5.3 Zircon U-Pb ages

Two samples from cumulate gabbro layers (13LX-17 and 13LX-19) and one gabbro sample from a vein (13LX-18) were selected for zircon geochronological study. The results of LA-ICP-MS U-Pb zircon analyses are listed in Table 2. The CL images and U-Pb concordia diagrams are shown in Fig. 9. Zircons from these gabbro samples are colorless and exhibit rectangle or irregular shapes with long axes of 50-120 μm and length/width ratios of 1.1-2.0. The CL images display a feature for zircons of magmatic origin with straight and wide oscillatory growth band (Fig. 9A).

Zircons from sample 13LX-17 have variable contents of U (58-1460 ppm) and Th (56-743 ppm) with Th/U ratios of 0.11-2.16. Six analyses yield apparent $^{206}Pb/^{238}U$ ages of 202-188 Ma with a weighted mean of 193±6 Ma (MSWD=2.4; Fig. 9B). Four analyses yield $^{206}Pb/^{238}U$ ages of 299-284 Ma with a weighted mean of 295±13 Ma (MSWD=0.26), other two give apparent $^{206}Pb/^{238}U$ ages of 406±6 Ma and 422±6 Ma, which would be the inherited ages of the CAOB (e.g., Song et al., 2015). One zircon gives 1767±25 Ma, which is derived from Precambrian basement (Table 2).

Zircons from gabbroic vein sample 13LX-18 have variable contents of U (111-1255

ppm) and Th (81-1669 ppm) with Th/U ratios of 0.17-1.86. Six analyses yield apparent $^{206}Pb/^{238}U$ ages of 160-153 Ma with a weighted mean of 156±3 Ma (MSWD=0.42; Fig. 9C), which is interpreted as the emplacement age of the vein. One analysis give apparent $^{206}Pb/^{238}U$ ages of 504±7 Ma, three analyses give a mean age of 1892±28 Ma (MSWD=0.002) and other five from an intercept age of 1039±50 Ma (Fig. 9C).

Zircons from sample 13LX-19 show highly variable U (49-1469 ppm) and Th (31-782 ppm) with Th/U ratios of 0.12-2.01. Eight analyses yield apparent $^{206}Pb/^{238}U$ ages of 188-171 Ma with a weighted mean of 179±4 Ma (MSWD=1.6; Fig. 9D), which is interpreted as the formation age of the Kedanshan ultramafic-mafic intrusion. Four analyses give apparent $^{206}Pb/^{238}U$ ages of 1809-1808 Ma, one give 1928±25 Ma and one 2154±27 Ma, which are xenocrysts derived from a Paleoproterozoic basement (Table 2).

On the basis of zircon analyses from the three gabbroic samples, the Kedanshan ultramafic-mafic intrusion formed in a long-lasting period of 193-179 Ma in Jurassic time. Zircon xenocrysts in these samples reveal that they are sourced from (1) a Paleoproterozoic basement with ages of 2100-1800 Ma associated with assembly of Columbia Supercontinent, (2) Grenvillian-aged orogeny of ~1000 Ma, and (3) the rocks of Paleozoic to Triassic ages from the CAOB.

6. Discussion

6.1 Petrogenesis: Alaskan-type ultramafic-mafic intrusion vs. ophiolite

Most researchers have considered the Kedanshan ultramafic-mafic intrusion as an ophiolite, related to the Paleo-Asian Ocean (e.g., Liang, 1994; Li et al., 2011). However,

lines of evidence in this study confirm it is an Alaskan-type ultramafic-mafic intrusion, formed in a super-subduction environment.

The Kedanshan ultramafic-mafic intrusion is an accumulated complex comprising dunite, pyroxene peridotite, olivine pyroxenite and gabbro/anorthosite without pillow lava and radiolite. Such a rock assemblage is different from all ophiolites of the Paleo-Asian Ocean in the eastern CAOB (Song et al., 2015). The variable compositions of olivine, clinopyroxene and chromian spinel show affinities with Alaskan-type intrusions (Fig. 4 to 6). The Fo values of olivine agree with those from typical Alaskan-type complexes worldwide (e.g., Irvine, 1976; Himmelberg et al., 1986; Clark, 1980; Rublee, 1994; Helmy and Moggesie, 2001; Pettigrew and Hattori, 2006).

6.2 Fractionation and accumulation

The Kedanshan ultramafic-mafic intrusion consists of several lithologies varying from dunite to gabbro. Increases of Al_2O_3 and CaO and decreases of compatible elements (Co, Cr and Ni) from dunite to gabbro indicate a crucial role for fractionation/accumulation of olivine, spinel, clinopyroxene and Ca-plagioclase (Fig.7).

In the AFM diagram (Fig.10), the studied samples plot in the arc-related ultramafic cumulative field. Samples from dunite show negative Eu and Sr anomalies, indicating olivine-controlled accumulation. Samples from olivine pyroxenite (e.g., 13LX-20 and 13LX-21) have La_N/Nd_N ratios less than 1.0 (N denotes chondrite normalization), suggesting Cpx-controlled accumulation (Guo et al., 2007). The gabbro samples display positive Eu and Sr anomalies, favoring Pl-controlled accumulation (Fig.8).

6.3 Nature of parental magma

In terms of field observations and petrography (Fig. 2 and 3), the crystallization sequences of minerals can be determined as olivine → chromian spinel → pyroxene → plagioclase, indicating that the parental magma of the Kedanshan ultramafic-mafic intrusion is hydrous (Gaetani, 1993). The early formed Mg-rich olivine and chromian spinel can be used to estimate the parental melt composition in equilibrium with the Kedanshan ultramafic-mafic intrusion. We use the equation of Maurel and Maurel (1982) to calculate Al_2O_3 contents of the parental melt: $(Al_2O_3)_{spinel} = 0.035 \times (Al_2O_3)_{melt}^{2.42}$. The FeO/MgO ratios of the parental melt are calculated by the equation of Roeder and Emslie (1970): $K_D = (FeO/MgO)_{olivine}/(FeO/MgO)_{melt}$, where the value of partition coefficient K_D is 0.30±0.03. The TiO_2 contents of the parental melt are calculated by the equation of Rollinson (2008): $(TiO_2)_{melt} = 1.0963 \times (TiO_2)_{spinel}^{0.7863}$.

Due to fractionation/accumulation, the MgO/FeO ratios calculated from olivine in pyroxene peridotite and olivine pyroxenite require the parental melt to be high-Mg with Mg# more than 64.1 (Table S1). The calculated Al_2O_3 and TiO_2 contents of the parental melt are 12.19-16.58 wt.% and 0.15-0.41 wt.%, respectively (Table S4). These calculations illustrate that the parental melt in equilibrium with the Kedanshan ultramafic-mafic intrusion is rich in Al and Mg and poor in Ti.

On the other hand, the high Cr_2O_3 and Wo contents of clinopyroxene, as well as high NiO and Fo from olivine, show these minerals crystallized in a hydrous basaltic magma system (Sisson and Grove, 1993; Eyuboglu et al., 2010). In addition, Al-rich chromian

spinel and An-rich plagioclase indicate that the liquidus composition was high in H_2O and Ca (Sisson and Grove, 1993; Cleason and Meurer, 2004), suggesting that the parental magma was relatively rich in Al, Mg, Ca and H_2O, and low in Ti.

The Kedanshan ultramafic-mafic intrusion show variable effects of crystal accumulation, so the whole-rock geochemistry can't represent the parental magma composition; instead it equals the sum of composition of the accumulative crystals and trapped melts (Bédard, 1994). In the following parts, we use the method of proposed by Guo et al. (2015) to estimate the parental magma composition of the Kedanshan ultramafic-mafic intrusion. Making by using olivine, the calculated formula can be expressed as:

$$\begin{cases} c_i^{rock} = \varphi^{Ol} c_i^{Ol} + \varphi^{Cpx} c_i^{Cpx} + \varphi^{Opx} c_i^{Opx} + \varphi^{TM} c_i^{TM}; \\ \dfrac{c_i^{Ol}}{c_i^{Cpx}} = \dfrac{D_i^{Ol/Melt}}{D_i^{Cpx/Melt}}, \dfrac{c_i^{Ol}}{c_i^{Opx}} = \dfrac{D_i^{Ol/Melt}}{D_i^{Opx/Melt}}, \dfrac{c_i^{Ol}}{c_i^{TM}} = D_i^{Ol/Melt}; \end{cases}$$

$$\Rightarrow c_i^{Ol} = \frac{c_i^{rock}}{\varphi^{Ol} + \varphi^{Cpx} \dfrac{D_i^{Cpx/Melt}}{D_i^{Ol/Melt}} + \varphi^{Opx} \dfrac{D_i^{Opx/Melt}}{D_i^{Ol/Melt}} + \varphi^{TM} \dfrac{1}{D_i^{Ol/Melt}}}$$

To simplify the calculation, the Kedanshan ultramafic-mafic intrusion is reduced to less than three-phase assemblages with a hypothetical trapped melt of 0-15 vol.%. The detailed calculation results with different trapped melts for studied samples are given in Table S5. The modal mineral compositions (φ) of the studied samples and partition coefficients (D) used in the calculation are given in Table S6 and S7, respectively. Here, we select the four samples (13LX-28, 11, 12 and 21) to estimate the composition of the parental magmas in equilibrium with the Kedanshan ultramafic-mafic intrusion. As

shown in Fig.11, the calculated parental magmas for every sample and different trapped melt fraction are enriched in LILEs, Th-U and LREEs, and depleted in Nb-Ta. These features suggest that the parental magmas of the Kedanshan ultramafic-mafic intrusion have arc geochemical affinities.

6.4 Long-lived superimposed subduction of the Mongol-Okhotsk and Paleo-Pacific oceans

Petrology and chemical composition of Kedanshan ultramafic-mafic intrusion suggests that the magma generation was in a subduction-related setting. The Cpx compositions also show geochemical affinities with arc basalts of a subduction-related setting (Fig. 12).

The studied region is located in the central Inner Mongolia region of the southeastern segment of the CAOB, which experienced Paleozoic orogeny by closure of the Paleo-Asian Ocean from Early Paleozoic to Triassic (Miao et al., 2007, 2008; Jian et al., 2012; Xu et al., 2013b, 2015; Song et al., 2015). To the east is the Mesozoic tectonism of the Paleo-Pacific Ocean that started to subduct westwards at ~200-190 Ma (e.g., Zhou et al., 2009; Wu et al., 2011; Zhou and Wilde, 2013), and to the north is the Mesozoic tectonism of the Mongol-Okhotsk Ocean (Zonenshain et al., 1990; Zorin, 1999; Tang et al., 2014; Wang et al., 2011, 2012, 2015a). However, the influence of these Mesozoic orogenies on the Kedanshan region remains equivocal, although some recent researches have supplied important perspectives (e.g., Xu et al., 2013a; Wang et al., 2015a).

389 The final closure of the Paleo-Asian Ocean was proposed to be finished in the
390 Triassic (>220 Ma) along the E-N-trending Solonker-Xar Moron suture zone (e.g., Jian et
391 al., 2012; Cao et al., 2013; Xu et al., 2013b, 2015; Zhao et al., 2014; Song et al., 2015). It
392 means that the formation time of the Kedanshan ultramafic-mafic intrusion postdates the
393 Paleo-Asian Ocean. That is, subduction of the Paleo-Asian Ocean was not responsible for
394 formation of the Kedanshan complex.
395 As an embayment of the Paleo-Pacific Ocean, the Mongol-Okhotsk Ocean existed in
396 the Paleozoic to Early Mesozoic between the Central Mongolia Massif and the Siberian
397 Craton (Zorin, 1999; Donskaya et al., 2013). Although the closure time of the
398 Mongol-Okhotsk Ocean is still under debate, the subduction of the Mongol-Okhotsk
399 Oceanic plate in the Late Paleozoic to Early Mesozoic has been confirmed (Donskaya et
400 al., 2013). Zorin (1999) suggested that the complete closure of the western part of the
401 Mongol-Okhotsk Ocean occurred in the Early to Middle Jurassic. In the eastern side of
402 the Mongol-Okhotsk tectonic belt, several early Mesozoic porphyry-type deposits
403 outcrop in the Chinese border area (Fig. 1A), such as the Taipingchuan porphyry Cu-Mo
404 deposit (~202 Ma, Chen et al., 2010), the Wunugetushan porphyry Cu-Mo deposit
405 (183-178 Ma, Chen et al., 2011) and the Badaguan porphyry Cu-Mo deposit (188-182 Ma,
406 Shen et al., 2010). These porphyry-type deposits are thought to result from subduction of
407 the Mongol-Okhotsk Ocean (e.g., Tang et al., 2014). In addition, some Early Mesozoic
408 granitoids related to subduction of the Mongol-Okhotsk Oceanic plate have been reported
409 along both sides of the eastern Mongol-Okhotsk orogenic belt (Orolmaa et al., 2008;

410 Jiang et al., 2010; Liu et al., 2010; Tang et al., 2014). The ocean appears to have closed as
411 a result of two subduction zones, dipping outwards under both adjacent continental
412 margins.

413 Paleomagnetic studies show that the Mongol-Okhotsk Ocean had not closed, and its
414 subduction still took place by ~155 Ma (Ren et al., 2016). Thus, with respect to the
415 spatial and temporal relations, we suggest that the Kedanshan ultramafic-mafic intrusion
416 might be long affected by the far-field effects of the southeastward subduction of the
417 Mongol-Okhotsk Ocean, during much of the Mesozoic.

418 Separate to the Mongol-Okhotsk Ocean, a S-N-trending accretionary belt with
419 ophiolites, high-pressure rocks and igneous rocks (210-150 Ma) has been reported in NE
420 China (Wu et al., 2005, 2011; Yu et al., 2012; Zhou and Wilde, 2013; Xu et al., 2013a; Li
421 et al., 2014; Zhou et al., 2009, 2014; Wang et al., 2015b; Guo et al., 2015; Niu et al.,
422 2015). These rocks suggest westward subduction of the Paleo-Pacific Oceanic plate
423 during the Mesozoic. Therefore, we suggest that the Paleo-Pacific subduction was also
424 responsible for formation of the Kedanshan ultramafic-mafic intrusion.

425 Taking these aspects into consideration, we consider that the plate between the
426 Mongol-Okhotsk Ocean and Paleo-Pacific Ocean (Fig. 13A) was affected by long-lived,
427 superimposed subduction during a long part of the Mesozoic (193-179 Ma). The
428 Mongol-Okhotsk Oceanic plate subducted toward the southeast beneath the Central
429 Mongolia Massif, and the Paleo-Pacific Oceanic plate subducted toward the northwest
430 beneath the Central Mongolia Massif in the same time. The long-lived superimposed

subduction (Fig. 13B) would form a large, triangle-shaped mantle wedge beneath Central Mongolia during the Mesozoic (193-179 Ma). Fluids/melts dehydrated from the subducted oceanic plate could remodify the overlying mantle wedge, and melting of the large mantle wedge produced hydrous ultramafic-mafic magmas along the superimposed subduction zones, recorded by the Kedanshan ultramafic-mafic intrusion.

7. Conclusions

(1) The Kedanshan ultramafic-mafic intrusion is a cumulate complex, similar to the Alaskan-type intrusions generated in arc settings.

(2) LA-ICP-MS zircon U-Pb data indicate that the ultramafic-mafic intrusion was formed in Jurassic times with an emplacement age between 193 to 179 Ma.

(3) The parental magmas for these Jurassic ultramafic-mafic rocks could be high-Mg, Al-rich and hydrous basaltic magma, originated from the partial melting of a depleted mantle wedge that was metasomatized by subduction zone fluids/melts.

(4) The formation of the Kedanshan ultramafic-mafic intrusion resulted from superimposed subduction between the Mongol-Okhotsk and the Paleo-Pacific oceanic plates during the Mesozoic.

Acknowledgements

We thank the staffs of the Geological Lab Center, China University of Geosciences, Beijing (CUGB), for their helps with major and trace element analyses, and zircon U-Pb dating. We thank Feng Guo, an anonymous reviewer and Editor-in-chief Mei-Fu Zhou for their constructive official review comments, which led to a better presentation of the final

product. This work was financially supported by the National Key Basic Research Program of China (2013CB429806) and the National Natural Science Foundation of China (grants 41572040, 41372060).

References

Barnes, S.J., Röeder, P.L., 2001. The range of spinel compositions in terrestrial mafic and ultramafic rocks. J. Petrol. 42, 2279-2302.

Beard, J.S., 1986. Characteristic mineralogy of arc-related cumulate gabbros: implications for the tectonic setting of gabbroic plutons and for andesite genesis. Geology 14, 848-851.

Burns L.E., 1985. The Border Ranges ultramafic and mafic complex, south-central Alaska: cumulate fractionates of island-arc volcanics. Can. J. Earth Sci. 22(7), 1020-1038.

Bédard, J.H., 1994. A procedure for calculating the equilibrium distribution of trace elements among the minerals of cumulate rocks, and the concentration of trace elements in the coexisting liquids. Chem. Geol. 118, 143-153.

Cao, H.H., Xu, W.L., Pei, F.P., Wang, Z.W., Wang, F., Wang, Z.J., 2013. Zircon U-Pb geochronology and petrogenesis of the Late Paleozoic-Early Mesozoic intrusive rocks in the eastern segment of the northern margin of the North China Block. Lithos 170-171, 191-207.

Chen, Z.G., Zhang, L.C., Lu, B.Z., Li, Z.L., Wu, H.Y., Xiang, P., Huang, S.W., 2010. Geochronology and geochemistry of the Taipingchuan copper-molybdenum deposit

in Inner Mongolia, and its geological significances. Acta Petrol. Sin. 26,1437-1449 (in Chinese with English abstract).

Chen, Z.G., Zhang, L.C., Wan, B., Wu, H.Y., Cleven, N., 2011. Geochronology and geochemistry of the Wunugetushan porphyry Cu-Mo deposit in NE China, and their geological significance. Ore Geol. Rev. 43, 92-105.

Cheng, Y.H., Teng, X.J., Li, Y.F., Li, M., Zhang, T.F., 2014. Early Permian East-Ujimqin mafic-ultramafic and granitic rocks from the Xing'an-Mongolian Orogenic belt, north china: origin, chronology, and tectonic implications. J. Asian Earth Sci. 96, 361-373.

Clark, T., 1980. Petrology of the Turnagain ultramafic complex, northwestern British Colombia. Can. J. Earth Sci. 17, 744-757.

Cleason, D.T., Meurer, W.P., 2004. Fractional crystallization of hydrous basaltic 'arctype' magmas and the formation of amphibole-bearing gabbroic cumulates. Contrib. Mineral. Petrol. 147, 288-304.

Cogné, J.P., Kravchinsky, V.A., Halim, N., Hankard, F., 2005. Late Jurassic-Early Cretaceous closure of the Mongol-Okhotsk Ocean demonstrated by new Mesozoic palaeomagnetic results from the Trans-Baïkal area (SE Siberia). Geophysical J. Royal Astronomical Soc. 163 (3), 813-832.

Conrad, W.K., Kay, R.W., 1984. Ultramafic and mafic inclusions from Adak island, crystallization history, and implications for the nature of primary magmas and crustal evolution in the Aleutian arc. J. Petrol. 25, 88-125.

494 DeBari, S.M., Coleman, R.G., 1989. Examination of the deep levels of an island arc:
495 evidence from the tonsina ultramafic-mafic assemblage, Tonsina, Alaska. J. Geophys.
496 Res. 94, 4373-4391.
497 DeBari, S.M., Kay, S.M., Kay, R.W., 1987. Ultramafic xenoliths from Adagdak volcano,
498 Adak, Aleutian Islands, Alaska: deformed igneous Cumulates from the Moho of an
499 Island Arc. J. Geol. 95, 329-341.
500 Dick, H.J.B., Bullen, T., 1984. Chromian spinel as a petrogenetic indicator in abyssal and
501 alpine-type peridotites and spatially associated lavas. Contrib. Mineral. Petrol. 86,
502 54-76.
503 Donskaya, T.V., Gladkochub, D.P., Mazukabzov, A.M., Ivanov, A.V., 2013. Late
504 paleozoic -mesozoic subduction-related magmatism at the southern margin of the
505 siberian continent and the 150 million-year history of the mongol-okhotsk ocean. J.
506 Asian Earth Sci. 62, 79-97.
507 Eyuboglu, Y., Dilek, Y., Bozkurt, E., Bektaş, O., Rojay, B., Şen, C., 2010. Structure and
508 geochemistry of an Alaskan-type ultramafic-mafic complex in the eastern Pontides,
509 NE Turkey. In: Santosh, M., Maruyama, S. (Eds.), A Tribute to Akiho Miyashiro:
510 Gondwana Res. 18, 230-252.
511 Farahat, E.S., Helmy, H.M., 2006. Abu Hamamid Neoproterozoic Alaskan-type
512 complex,south Eastern Desert, Egypt. J. Afr. Earth Sci. 45, 187-197.
513 Gaetani, G.A., Grove, T.L., Bryan, W.B., 1993. The influence of water on the
514 petrogenesis of subduction-related igneous rocks. Nature 365, 332-334.

Gill, J.B., 1981. Orogenic Andesites and Plate Tectonics. Springer Verlag, New York, p. 385.

Grove, T.L., Elkins Tanton, L.T., Parman, S.W., Cartterjee, N., Muntener, O., Gaetani, G.A., 2003. Fractional crystallization and mantle melting controls on calk-alkaline differ-entiation trends. Contrib. Mineral. Petrol. 145, 515-533.

Guo, F., Li, H.X., Fan, W.M., Li, J.Y., Zhao, L., Huang, M.W., 2016. Variable sediment flux in generation of Permian subduction-related mafic intrusions from the Yanbian region, NE China. Lithos 261, 195-215.

Guo, F., Li, H.X., Fan, W.M., Li, J.Y., Zhao, L., Huang, M.W., Xu, W.L., 2015. Early Jurassic subduction of the Paleo-Pacific Ocean in NE China: Petrologic and geochemical evidence from the Tumen mafic intrusive complex. Lithos 224-225, 46-60.

Guo, F., Nakamura, E., Fan, W.M., Kobayoshi, K., Li, C.W., 2007. Generation of Palaeocene adakitic andesites by magma mixing; Yanji Area, NE China. J. Petrol. 48, 661-692.

Helmy, H.M., EI Mahallawi, M.M., 2003. Gabbro Akarem mafic-ultramafic complex,Eastern Desert, Egypt: a late Precambrian analogue of Alaskan-type complexes. Mineral. Petrol. 77, 85-108.

Helmy, H.M., Moggesie, A., 2001. Gabbro Akarem, Eastern Desert, Egypt: Cu-Ni-PGE mineralization in a concentrically zoned mafic-ultramafic complex. Miner. Deposita 36, 58-71.

536 Helmy, H.M., Yoshikawa, M., Shibata, T., Arai, S., Kagami, H., 2015. Sm-Nd and Rb-Sr
537 isotope geochemistry and petrology of Abu Hamamid intrusion, Eastern Desert,
538 Egypt: an Alaskan-type complex in a back arc setting. Precambrian Res. 258,
539 234-246.
540 Himmelberg, G.R., Loney, R.A., 1995. Characteristics and petrogenesis of Alaskan-type
541 ultramafic-mafic intrusions, Southeastern Alaska. US Geological Survey
542 Professional Paper.
543 Himmelberg, R.G., Loney, R.A., Craig, J.T., 1986. Petrogenesis of the ultramafic
544 complex at the Blashke Islands, southeastern Alaska. U.S. Geological Survey
545 Bulletin 1662, 1-14.
546 Irvine, T.N., 1967. Chromian spinel as a petrogenetic indicator: part 2. Petrologic
547 applications. Can. J. Earth Sci. 4, 71-103.
548 Irvine, T.N., 1974. Petrology of the Duke Island ultramafic complex southern Alaska.
549 Geological Society of Am. Mineral. 138, 240.
550 Irvine, T.N., 1976. Alaskan-type Ultramafic-gabbro Bodies in the Aiken Lake, McConnel
551 Creek, and Toodagoone Map-areas. Geological Survey of Canada Paper 76-1A pp.
552 76-81.
553 Ishiwatari, A., Ichiyama, Y., 2004. Alaskan-type plutons and ultramafic lavas in Far East
554 Russia, Northeast China, and Japan. International Geolo. Rev. 46, 316-331.
555 Jian, P., Kröner,A., Windley,B.F., Shi,Y., Zhang,W., Zhang, L., Yang, W., 2012.
556 Carboniferous and Cretaceous mafic-ultramafic massifs in Inner Mongolia (China):

557 A SHRIMP zircon and geochemical study of the previously presumed integral
558 “Hegenshan ophiolite”, Lithos 142-143, 48-66.
559 Jiang, S.H., Nie, F.J., Su, Y.J., Bai, D.M., Liu, Y.F., 2010. Geochronology and Origin of
560 the Erdenet Superlarge Cu-Mo Deposit in Mongolia. Acta Petrol. Sin. 31, 289-306
561 (in Chinese with English abstract).
562 Kamenetsky V.S,, Gurenko A.A,, Kerr A.C., 2010. Composition and temperature of
563 komatiite melts from Gorgona Island, Colombia, constrained from olivine-hosted
564 melt inclusions. Geology 38(11):1003-1006.
565 KePezhinskas, P., Mcdermott, F., Defant, M. J., Hochstaedter, A., Drummond, M. S.,
566 Hawkesworth, C. J., Koloskov, A., Maury, R.C., Bellon, H., 1997. Trace element
567 and Sr-Nd-Pb isotopic constraints on a three-component model of kamchatka arc
568 petrogenesis. Geochim. Cosmochim. Acta 61, 577-600.
569 Kim, N.K., Choi, S.H. 2016. Petrogenesis of late Triassic ultramafic rocks from the
570 Andong ultramafic complex, South Korea. Lithos 264, 28-40.
571 Krause J., Brügmann G.E., Pushkarev E.V., 2007. Accessory and rock forming minerals
572 monitoring the evolution of zoned mafic-ultramafic complexes in the Central Ural
573 Mountains. Lithos 95:19-42.
574 Le Bas, M.J., 1962. The role of aluminum in igneous clinopyroxenes with relation to their
575 parentage. Am. J. Sci. 260, 267-288.
576 Li, H., Liu, Q., Hou, Q.L., Xu, H.H., Zhu, M.X., Zeng, G.H., 2011. Distribution and
577 fractionation of Platinum-group elements in mantle peridotites from Kedanshan

578 ophiolite，Inner Mongolia. Acta Petrol. Sin. 27, 1759-1769 (in Chinese with English
579 abstract).
580 Li, J.Y., Guo, F., Li, C.W., Li, H.X., Zhao, L., 2014. Neodymium isotopic variations of
581 Late Paleozoic to Mesozoic I- and A-type granitoids in NE China: implications for
582 tectonic evolution. Acta Petrol. Sin. 30, 1995-2008 (in Chinese with English
583 abstract).
584 Li, S., Wang, T., Tong, Y., 2010. Spatial-temporal distribution and tectonic settings of
585 Early Mesozoic granitoids in the middle-south segment of the Central Asia Orogenic
586 System. Acta Petrol. Mineral. 29 (6), 642-662 (in Chinese with English abstract).
587 Li, Y.J., Wang, J.F., Dong, P.P., Liu, Y.C., Liu, D.W., Bai, H., 2012a. Recognition of
588 diyanmiao ophiolite in xi u jimqin banner, inner mongolia. Acta Petrol. Sin. 28,
589 1282-1290 (in Chinese with English abstract).
590 Li, C., Thakurta, J., Ripley, E.M., 2012b. Low-Ca contents and kink-banded textures are
591 not unique to mantle olivine: evidence from the Duke Island Complex, Alaska.
592 Mineral. Petrol. 104(3):147-153.
593 Liang, R.X., 1994. The features of ophiolites in the central sector of Inner Mongolia and
594 its geological significance. Regional Geology of China 1, 37-45 (in Chinese with
595 English abstract).
596 Liu, Y.F., Nie, F.J., Jiang, S.H., Xue, J., Hou, W.R., Yun, F., 2010. The Geochronology
597 and Geochemical Features of Ore-hosting Granite in the Aryn nuur Molybdenum
598 Deposit, Mongolia. Acta Geosci. Sin. 31 (03), 343-349 (in Chinese with English

599 abstract).
600 Loucks, R.R., 1990. Discrimination of ophiolitic from nonophiolitic ultramafic-mafic
601 allochthons in orogenic belts by the Al/Ti ratio in clinopyroxene. Geology 18,
602 346-349.
603 Ludwig, K.R., 2003. User's manual for Isoplot 3.00: a geochronological toolkit for
604 Microsoft Excel (No. 4). Kenneth R. Ludwig.
605 Maurel, C., Maurel, P., 1982. Étude expérimentale de la distribution de l‘aluminiu mentre
606 bain silicaté basique et spinelle chromifère. Implications pétrogénétiques: teneur
607 enchrome des spinelles. Bull. Minéral. 105, 197-202.
608 Meibom, A., Sleep, N.H., Chamberlain, C.P., Coleman, R.G., Frel, R., Hren, M.T.,
609 Wooden, J.L., 2002. Re-Os isotopic evidence for long-lived heterogeneity and
610 equilibration processes in the Earth's upper mantle. Nature 419, 705-708.
611 Miao, L., Zhang, F., Fan, W.M., Liu, D., 2007. Phanerozoic evolution of the Inner
612 Mongolia Daxinganling orogenic belt in North China: constraints from
613 geochronology of ophiolites and associated formations. Geological Society London
614 Special Publications 280, 223-237.
615 Miao, L.C., Fan, W.M., Liu, D.Y., Guo, F., 2008. Geochronology and geochemistry of the
616 Hegenshan ophiolitic complex: Implications for late-stage tectonic evolution of the
617 Inner Mongolia-Daxinganling Orogenic Belt, China. J. Asian Earth Sci. 32, 348-370.
618 Morimoto, N., 1988. Nomenclature of Pyroxenes. Mineral. Petrol. 39, 55-76.
619 Murray, C.G., 1972. Zoned ultramafic complexes of the Alaskan type: feeder pipes of

620 andesitic volcanoes. In: Shagam, R.E., et al. (Eds.). Studies in Earth and Space
621 Science (Hess Volume), Geologic Society of America Memoir, vol. 132, pp.
622 313-335.
623 Niu, Y.L., Gilmore, T., Mackie, S., Greig, A., Bach, W., 2002. Mineral chemistry,
624 wholerock compositions and petrogenesis of ODP Leg 176 gabbros: data and
625 discussion. In: Natland, J.H., Dick, H.J.B., Miller, D.J., Von Herzen, R.P. (Eds.),
626 Proc. ODP: Sci. Results, vol. 176 1-60 pp.
627 Niu, Y.L., Liu, Y., Xue, Q.Q., Shao, F.L., Chen, S., Duan, M., et al., 2015. Exotic origin
628 of the Chinese continental shelf: new insights into the tectonic evolution of the
629 western Pacific and eastern China since the Mesozoic. Sci. Bull. 60(18):1598-1616.
630 Niu, Y.L., O'Hara, M.J., 2009. MORB mantle hosts the missing Eu (Sr, Nb, Ta and Ti) in
631 the continental crust: New perspectives on crustal growth, crust–mantle
632 differentiation and chemical structure of oceanic upper mantle. Lithos 112, 1-17.
633 Orolmaa, D., Erdenesaihan, G., Borisenko, A.S., Fedoseev, G.S., Babich, V.V., Zhmodik,
634 S.M., 2008. Permian-Triassic granitoid magmatism and metallogeny of the Hangayn
635 (central Mongolia). Rus. Geolo. Geophysi. 49, 534-544.
636 Pettigrew, N.T., Hattori, K.H., 2006. The Quetico Intrusions of Western Superior
637 Province: Neo-Archean examples of Alaskan/Ural-type mafic-ultramafic intrusions.
638 Precambrian Res. 149, 21-42.
639 Polat, A., Appel, P.W.U., Fryer, B.J., 2011. An overview of the geochemistry of
640 Eoarchean to Mesoarchean ultramafic to mafic volcanic rocks, SW Greenland:

641 Implications for mantle depletion and petrogenetic processes at subduction zones in
642 the early Earth. Gondwana Res. 20, 255-283.
643 Ren, Q., Zhang, S.H., Wu, H.C., Liang, Z.K., Miao, X.J., Zhao, H.Q., Li, H.Y., Yang,
644 T.S., Pei, J.L., Davis, G.A., 2016. Further paleomagnetic results from the ~ 155 Ma
645 Tiaojishan Formation, Yanshan Belt, North China, and their implications for the
646 tectonic evolution of the Mongol-Okhotsk suture. Gondwana Res. 35:180-191.
647 Ripley, E.M., 2009. Magmatic sulfide mineralization in Alaskan-type complexes. In: Li,
648 C.S., Ripley, E.M. (Eds.), New Development in Magmatic Ni-Cu and PGE Deposits
649 7. Geological Publishing House, Beijing, pp. 219-228.
650 Roeder, P.L., Emslie, R.F., 1970. Olivine-liquid equilibrium. Contrib. Mineral. Petrol. 29,
651 275-289.
652 Rollinson, H., 2008. The geochemistry of mantle chromitites from the northern part of the
653 Oman ophiolite: inferred parental melt compositions. Contrib. Mineral. Petrol. 156,
654 273-288.
655 Rublee, V.J., 1994. Chemical Petrology, Mineralogy and Structure of the Tulameen
656 Complex, Princeton Area, British Colombia. Unpublished M.Sc. Thesis. University
657 of Ottawa, Canada, p. 179.
658 Shen, C.L., Zhang, M., Yu, X.Q., Chen, W.G., Gao, W.Y., Zhou, W.C., 2010. New
659 progresses in exploration of molybdenum deposits and analysis of mineralization
660 prospect in Inner Mongolia. Geolo. Explor. 46, 561-575 (in Chinese with English
661 Abstract).

662 Sisson, T.W., Grove, T.L., 1993. Experimental investigations of the role of H_2O in
663 calcalkaline differentiation and subduction zone magmatism. Contrib. Mineral.
664 Petrol. 113, 143-166.
665 Snoke, A.W., Quick, J.E., Bowman, H.R., 1981. Bear mountain igneous complex,
666 Klamath mountains, California: an ultrabasic to silicic cale-alkaline suite. J. Petrol.
667 22, 501-552.
668 Song, S.G., Niu, Y.L., Wei, C.J., Ji, J.Q., Su, L., 2010. Metamorphism, anatexis, zircon
669 ages and tectonic evolution of the Gongshan block in the northern Indochina
670 continent-an eastern extension of the Lhasa Block. Lithos 120, 327-346.
671 Song, S.G., Wang, M.M., Xu, X., Wang, C., Niu, Y.L., Allen, M.B., Su, L., 2015.
672 Ophiolites in the Xing'an-Inner Mongolia accretionary belt of the CAOB:
673 Implications for two cycles of seafloor spreading and accretionary orogenic events.
674 Tectonics 34, 2221-2245.
675 Sorokin, A.A., Yarmolyuk, V.V., Kotov, A.B., 2004. Geochronology of Triassic-Jurassic
676 granitoids in the southern framing of the Mongol-Okhotsk foldbelt and the problem
677 of Early Mesozoic granite formation in Central and Eastern Asia. Dokl. Earth Sci.
678 399, 1091-1094.
679 Su, B.X., Qin, K.Z., M., Santosh., Sun, H., Tang, D.M., 2013. The Early Permian
680 mafic-ultramafic complexes in the Beishan Terrane, NW china: Alaskan-type
681 intrusives or rift cumulates? J. Asian Earth Sci. 66, 175-187.
682 Sun, S.S., Mcdonough, W.F., 1989. Chemical and isotopic systematics of oceanic basalts;

683 implications for mantle composition and processes. Geological Society London
684 Special Publications 42, 313-345.
685 Tang, J., Xu, W.L., Wang, F., Wang, W., Xu, M.J., Zhang, Y.H., 2014. Geochronology and
686 geochemistry of Early-Middle Triassic magmatism in the Erguna Massif, NE China:
687 constraints on the tectonic evolution of the Mongol-Okhotsk Ocean. Lithos 184-187,
688 1-16.
689 Thakurta, J., Ripley, E.M., Li,C., 2008. Geochemical constraints on the origin of sulfide
690 mineralization in the Duke Island Complex, southeastern Alaska. Geochem.
691 Geophysi. Geosys. 9, 3562-3585.
692 Tistl, M., Burgath, K.P., Hohndorf, A., Kreuzer, H., Munoz, R., Salinas, R., 1994. Origin
693 and emplacement of Tertiary ultramafic complexes in northwest Colombia:
694 Evidence from geochemistry and K-Ar, Sm-Nd and Rb-Sr isotopes. Earth Planet.
695 Sci. Lett. 126, 41-59.
696 Tong, Y., Hong, D.W., Wang, T., Shi, X.J., Zhang, J.J., Zeng, T., 2010. Spatial and
697 temporal distribution of granitoids in the middle segment of the Sino-Mongolian
698 Border and its tectonic and metallogenic implications. Acta Geosci. Sin. 31, 395-412
699 (in Chinese with English abstract).
700 Wang, F., Xu, W.L., Xu, Y.G., Gao, F.H., Ge, W.C., 2015b. Late Triassic bimodal igneous
701 rocks in eastern Heilongjiang Province, NE China: implications for the initiation of
702 subduction of the Paleo-Pacific Plate beneath Eurasia. J. Asian Earth Sci. 97,
703 406-423.

Wang, T., Guo, L., Zhang, L., Yang, Q.D., Zhang, J.J., Tong, Y., Ye, K., 2015a. Timing and evolution of Jurassic-Cretaceous granitoid magmatisms in the Mongol-Okhotsk belt and adjacent areas, NE Asia: Implications for transition from contractional crustal thickening to extensional thinning and geodynamic settings. J. Asian Earth Sci. 97, 365-392.

Wang, T., Guo, L., Zheng, Y.D., Donskaya, T., Gladkochub, D., Zeng, l.S., 2012. Timing and processes of late Mesozoic mid-lower-crustal extension in continental NE Asia and implications for the tectonic setting of the destruction of the North China Craton: mainly constrained by zircon U-Pb ages from metamorphic core complexes. Lithos 154, 315-345.

Wang, T., Zheng, Y.D., Zhang, J.J., Zeng, l.S., Donskaya, T., Guo, L., Li, J.B., 2011. Pattern and kinematic polarity of late Mesozoic extension in continental NE Asia: perspectives from metamorphic core complexes. Tectonics 30 (6), TC6007, doi:10.1029/2011TC002896.

Wu, F.Y., Yang, J.H., Wilde, S.A., Zhang, X.O., 2005. Geochronology, petrogenesis and tectonic implications of Jurassic granites in the Liaodong Peninsula, NE China, Chem. Geol. 221,127-156.

Wu, F.Y., Sun, D.Y., Ge, W.C., Zhang, Y.B., Grant, M.L., Wilde, S.A., Jahn, B.M., 2011. Geochronology of the Phanerozoic granitoids in northeastern China. J. Asian Earth Sci. 41, 1-30.

Wu, F.Y., Zhao, G.C., Sun, D.Y., Wilde, S.A., Yang, J.H., 2007. The Hulan Group: its role

725 in the evolution of the Central Asian Orogenic Belt of NE China. J. Asian Earth Sci.
726 30, 542-556.
727 Xiao, W.J., Windley, B.F., Hao, J., Zhai M., 2003. Accretion leading to collision and the
728 Permian Solonker suture, Inner Mongolia, China: Termination of the Central Asian
729 Orogenic Belt. Tectonics 22, 1069, doi:10.1029/2002TC001484.
730 Xiao, W.J., Windley, B.F., Huang, B.C., Han, C.M., Yuan, C., Chen, H.L., Sun, M., Sun,
731 S., Li, J.L., 2009. End-Permian to mid-Triassic termination of the accretionary
732 processes of the southern Altaids: Implications for the geodynamic evolution,
733 Phanerozoic continental growth, and metallogeny of Central Asia. International J.
734 Earth Sci. 98, 1189-1217.
735 Xu, W.L., Pei, F.P., Wang, F., Meng, E., Ji, W.Q., Yang, D.B., Wang, W., 2013a.
736 Spatial-temporal relationships of Mesozoic volcanic rocks in NE China: constraints
737 on tectonic overprinting and transformations between multiple tectonic regimes. J.
738 Asian Earth Sci. 74, 167-193.
739 Xu, B., Charvet, J., Chen Y., Zhao, P., Shi, G.Z., 2013b. Middle Paleozoic convergent
740 orogenic belts in western Inner Mongolia (China): framework, kinematics,
741 geochronology and implications for tectonic evolution of the Central Asian Orogenic
742 Belt. Gondwana Res. 23, 1342-1364.
743 Xu, B., Zhao, P., Wang, Y.Y., Liao, W., Luo, Z.W., Bao, Q.Z., Zhou, Y.H., 2015. The
744 pre-Devonian tectonic framework of Xing’an-Mongolia orogenic belt (XMOB) in
745 north China. J. Asian Earth Sci. 97, 183-196.

Yu, J.J., Wang, F., Xu, W.L., Gao, F.H., Pei, F.P., 2012. Early Jurassic mafic magmatism in the Lesser Xing'an-Zhangguangcai Range, NE China, and its tectonic implications: Constraints from zircon U-Pb chronology and geochemistry. Lithos 142-143, 256-266.

Zhang, Q., 2014. Classification of mafic-ultramafic rocks and their tectonic significance. Cinaese Journal of Geology 49, 982-1017 (in Chinese with English abstract).

Zhang, Z.C., Hao, Y.L., Wang, F.S., Mahoney, J.J., 2004. Petrology, Mineralogy and Geochemistry of the Emeishan Continental Flood Basalts, SW China: Evidence for Activity of Mantle Plumes. Acta Geolo. Sin. 78, 40-51 .

Zhang, Z.C., Mao, J.W., Wang, F.S., Hao, Y.L., Mahoney, J.J., 2005. Mantle plume activity and melting conditions: Evidence from olivines in picritic-komatiitic rocks from the Emeishan Large Igneous Province, southwestern China. Acta Geolo. Sin. 28, 171-176.

Zhou, J.B., Cao, J.L., Wilde, S.A., Zhao, G.C., Zhang, J.J., Wang, B., 2014. Paleo-Pacific subduction-accretion: evidence from Geochemical and U-Pb zircon dating of the Nadanhada accretionary complex, NE China. Tectonics 33, 2444-2466.

Zhou, J.B., Wilde, S.A., 2013. The crustal accretion history and tectonic evolution of the NE China segment of the Central Asian Orogenic Belt. Gondwana Res. 23, 1365-1377.

Zhou, J.B., Wilde, S.A., Zhang, X.Z., Zhao, G.C., Zheng, C.Q., Wang, Y.J., Zhang, X.H., 2009. The onset of Pacific margin accretion in NE China: evidence from the

767 Heilongjiang high-pressure metamorphic belt. Tectonophysics 478, 230-246.
768 Zonenshain, L.P., Kuzmin, M.I., Natapov, L.M., 1990. Geologyof the USSR: A Plate
769 Tectonic Synthesis. American Geophysical Union, Geodynamics Series, 21.
770 Zorin, Y.A., 1999. Geodynamics of the western part of the Mongolia-Okhotsk collisional
771 belt, Trans-Baikal region (Russia) and Mongolia. Tectonophysics 306 (1), 33-56.
772 Zhao, P., Fang, J.Q., Xu, B., Chen, Y., Faure, M., 2014. Early Paleozoic tectonic
773 evolution of the Xing-Meng Orogenic Belt: Constraints from detrital zircon
774 geochronology of western Erguna-Xing'an Block, North China. J. Asian Earth Sci.
775 95(38):136-146.

Figure Captions

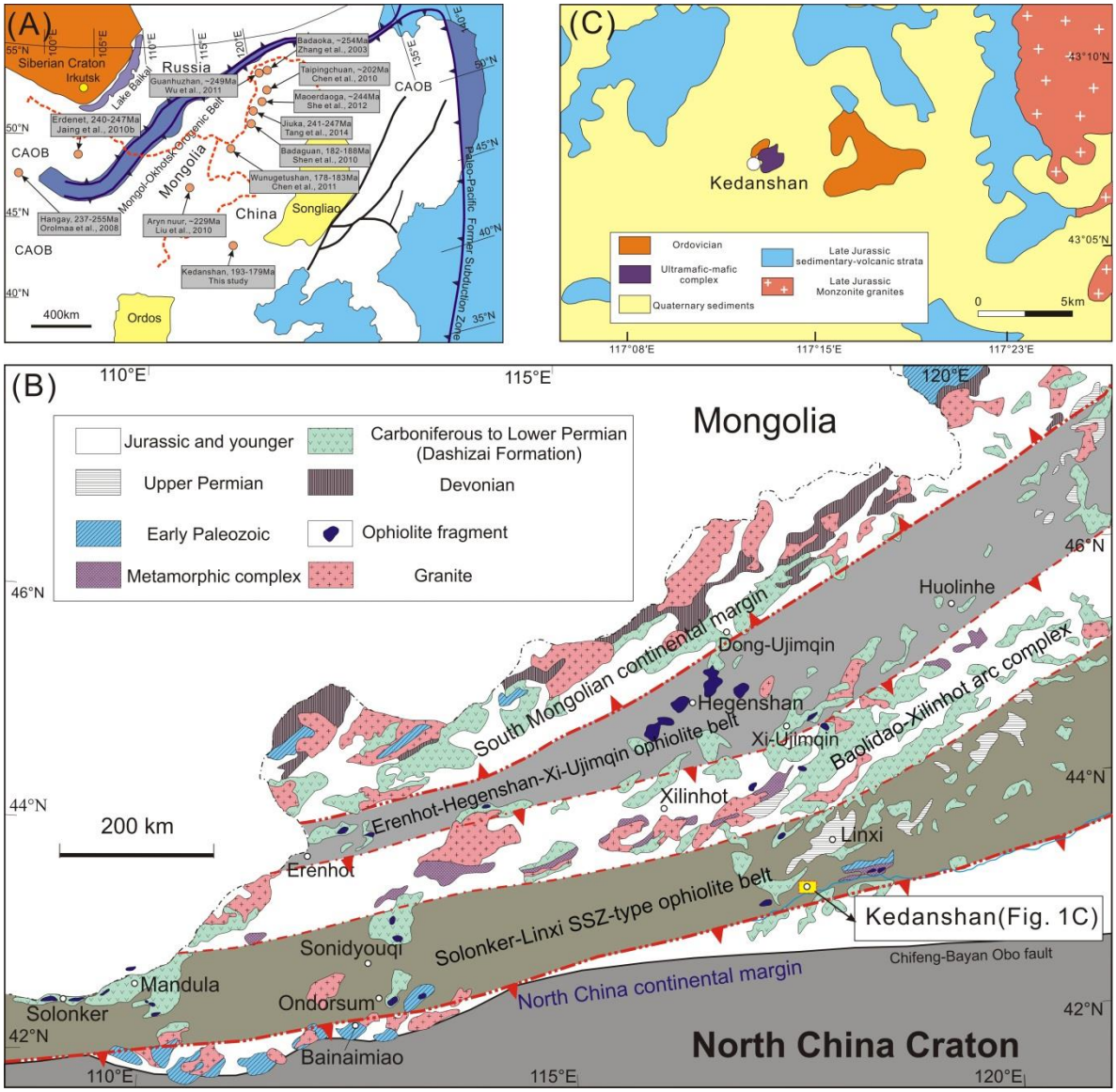

Fig. 1. (A) Sketch map showing the Mongol-Okhotsk orogenic belt, Paleo-Pacific former subduction zone, and distribution of the Late Triassic to Early Jurassic igneous rocks and porphyry Cu-Mo deposits, modified after Li et al. (2010) and Wang et al. (2012). (B) Geological map of the XIMAB modified after Miao et al. (2007) and Song et al. (2015). (C) Simplified geological map of the Kedanshan area.

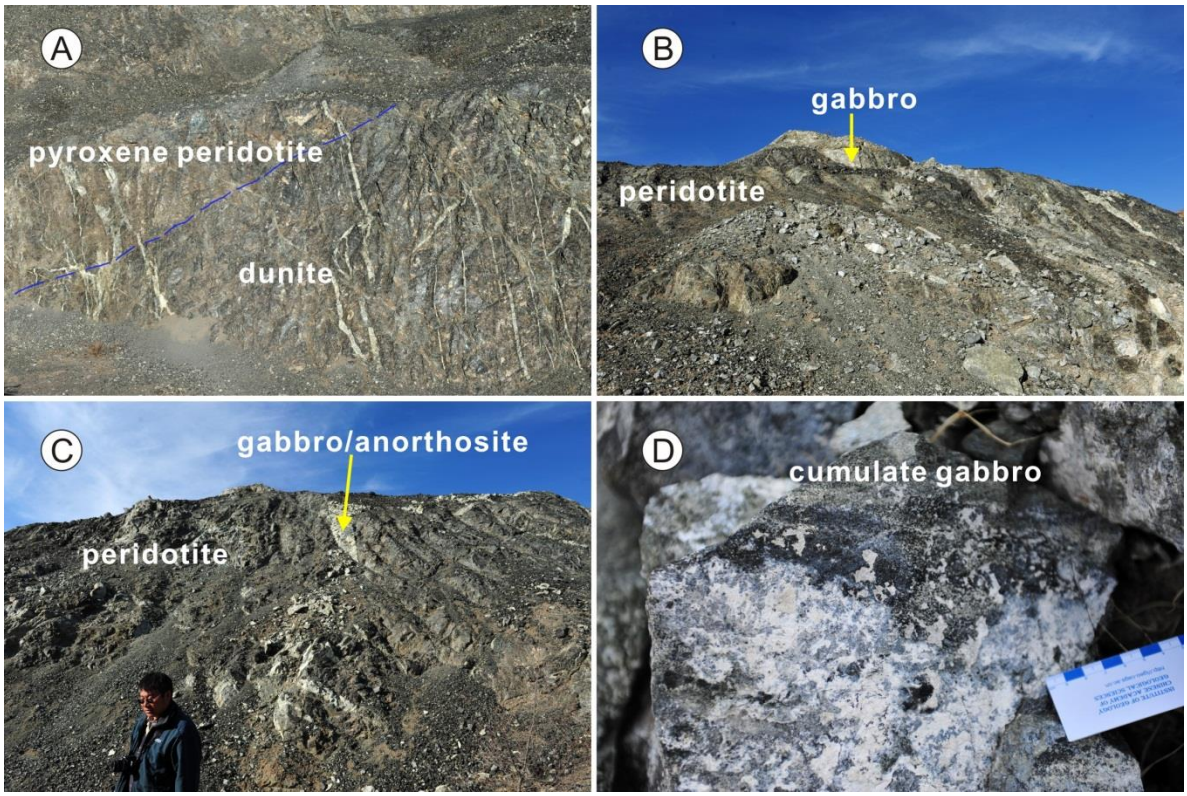

Fig. 2. Field photos from the Kedanshan ultramafic-mafic intrusion. (A) Field occurrence of dunite and pyroxene peridotite, both are strongly serpentinized. The white veins are gabbro/anorthosite. (B) Peridotite interlayered with gabbro. (C) Gabbro/anorthosite veins cutting the peridotite layers. (D) Cumulate gabbro with layered structure.

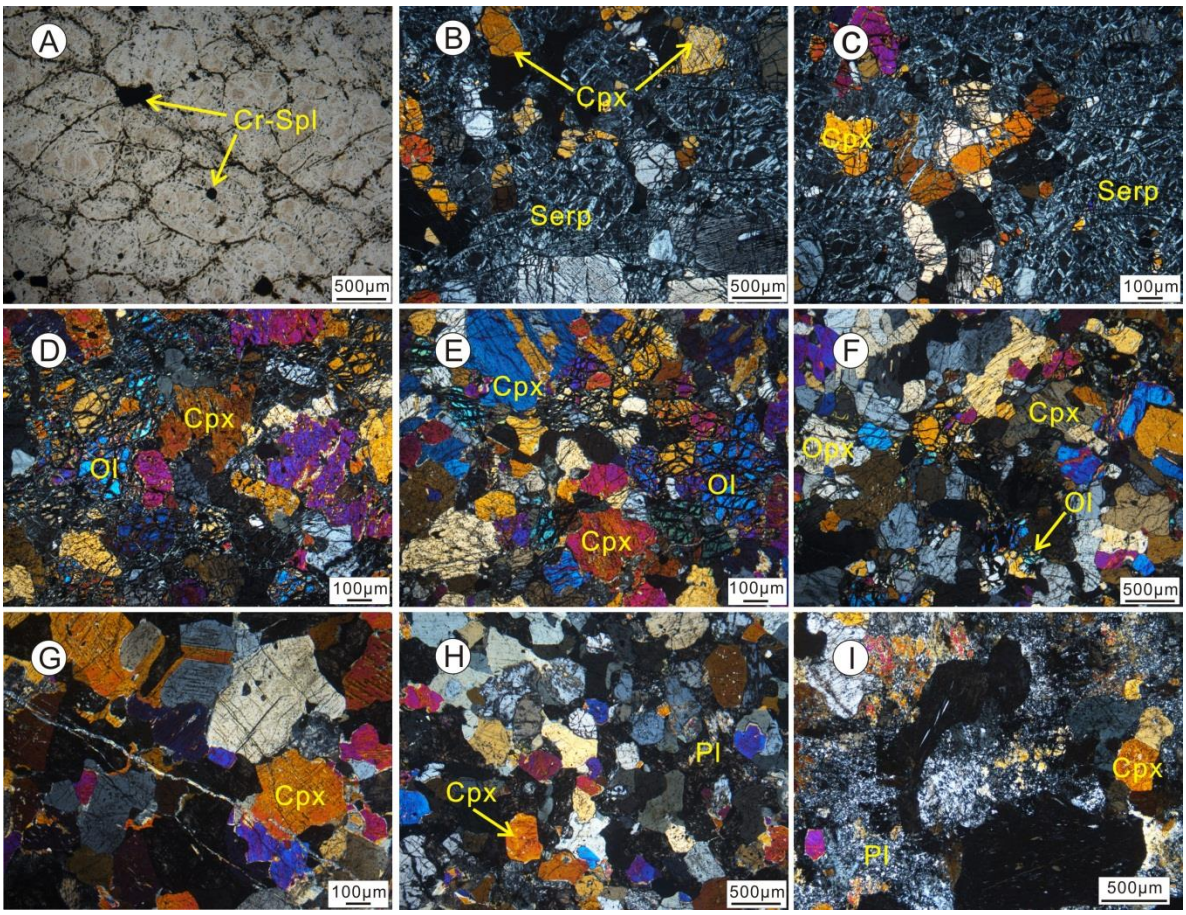

788

789 **Fig. 3.** Photomicrographs from the Kedanshan ultramafic-mafic intrusion. (A) Strongly serpentinized

790 cumulate dunite with irregular chromian spinel without pyroxene (13LX-26). (B) Strongly

791 serpentinized dunite with ~5 vol.% clinopyroxene (13LX-14). (C) Strongly serpentinized dunite with

792 ~8 vol.% clinopyroxene (13LX-14). (D) Pyroxene peridotite with olivine > pyroxene (13LX-22). (E)

793 Pyroxene peridotite with olivine ≈ pyroxene (13LX-21). (F) Olivine-bearing pyroxenite with olivine

794 << pyroxene (13LX-20). (G) Pl-poor pyroxenite with plagioclase << pyroxene (13LX-18). (H)

795 Cumulate gabbro with plagioclase < pyroxene (13LX-27). (I) Pl-rich cumulate gabbro with

796 plagioclase >> pyroxene (13LX-19).

797

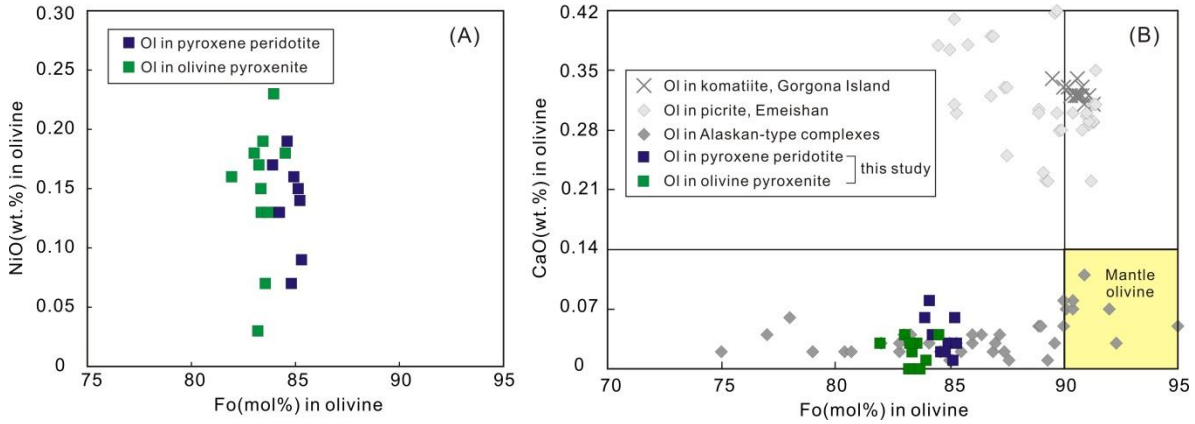

Fig. 4. (A) NiO versus Fo number diagram and (B) plot of CaO versus Fo number (modified after Li et al., 2012b) for olivines from the Kedanshan ultramafic-mafic intrusion. Komatiite data from Kamenetsky et al. (2010); picrite data from Zhang et al. (2004, 2005); Alaskan-type complexes data from Li et al. (2012b) and Krause et al. (2007).

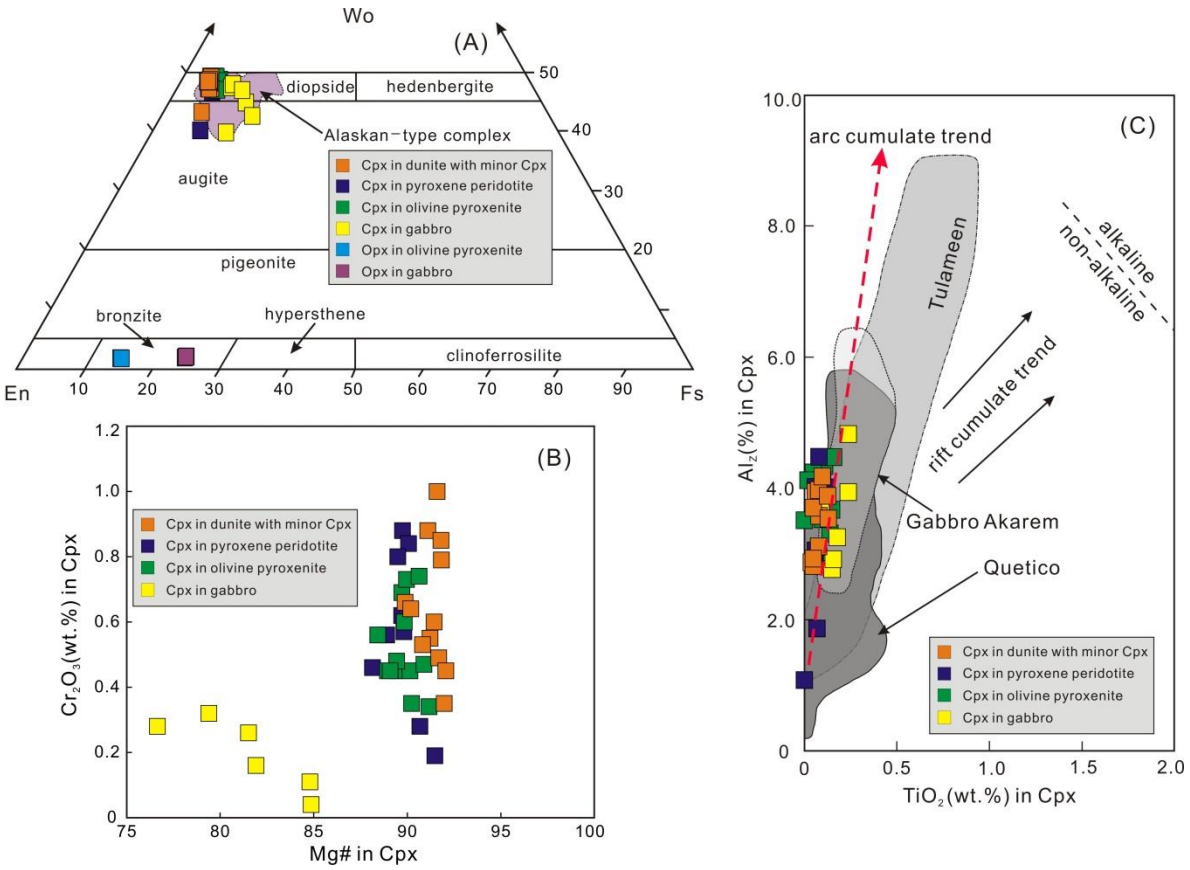

Fig. 5. (A) Wo-En-Fs diagram (Morimoto, 1988) for pyroxenes from the Kedanshan ultramafic-mafic intrusion. (B) Variation diagram of Mg# versus Cr_2O_3 wt.% for clinopyroxenes from the Kedanshan ultramafic-mafic intrusion. (C) Alz (percentage of tetrahedral sites occupied by Al) versus TiO_2 (wt.%) plot for clinopyroxenes from the Kedanshan ultramafic-mafic intrusion. The gray fields are typical Alaskan-type complexes worldwide. Quetico data are from Pettigrew and Hattori (2006), Tulameen from Rublee (1994), Gabbro Akarem from Helmy and EI Mahallawi (2003). Alkaline and non-alkaline field, arc cumulate trend and rift cumulate trend are from Le Bas (1962) and Loucks (1990).

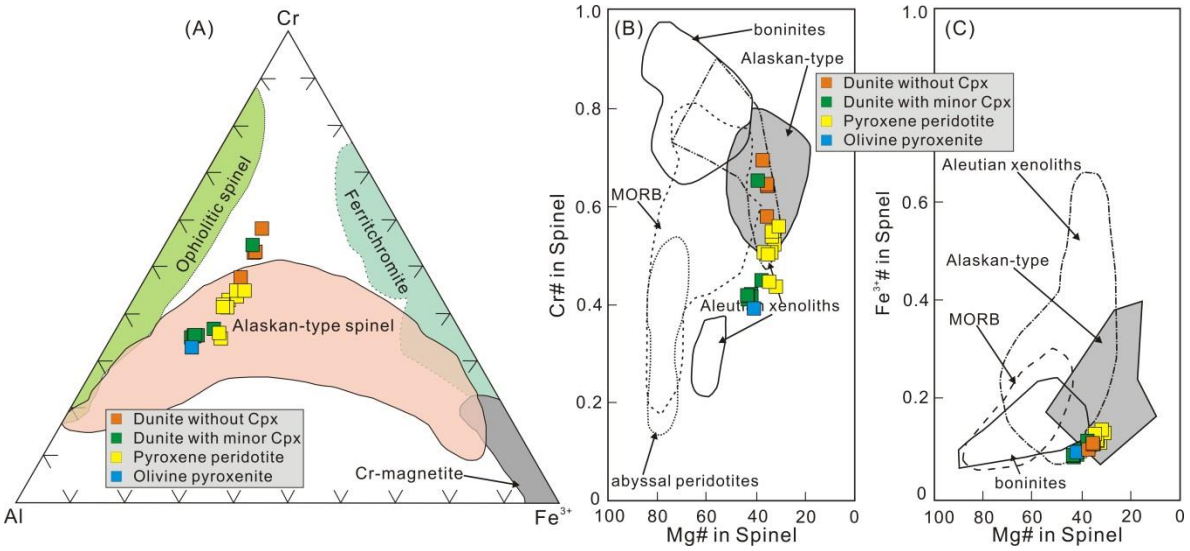

816

817 **Fig. 6.** (A) Cr-Al-Fe^{3+} triangle plot of chromian spinels from the Kedanshan ultramafic-mafic

818 intrusion. Discriminating fields from Irvine (1967), Barnes and Röeder (2001), Helmy and EI

819 Mahallawi (2003) and Farahat and Helmy (2006). (B) Plot of Cr# versus Mg# of chromian spinels

820 from the Kedanshan ultramafic-mafic intrusion. (C) Plot of Fe^{3+}# versus Mg# of chromian spinels

821 from the Kedanshan ultramafic-mafic intrusion. MORB and boninite fields from Barnes and Roeder

822 (2001), abyssal peridotite field from Dick and Bullen (1984), Alaskan-type field from Burns (1985)

823 and Himmelberg and Loney (1995), Aleutian pyroxenite and gabbro xenoliths fields from Conrad and

824 Kay (1984), DeBari et al. (1987), DeBari and Coleman (1989).

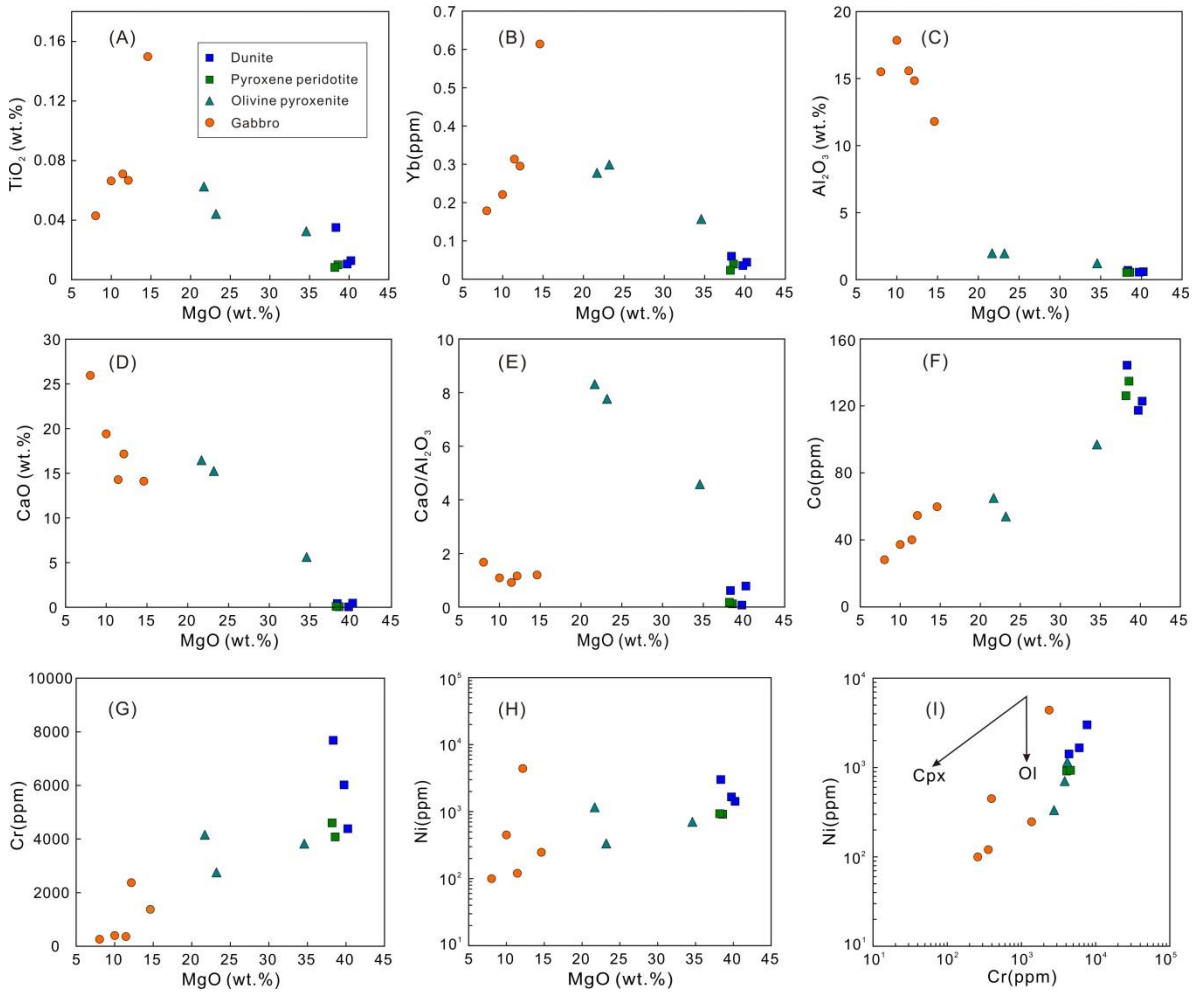

Fig. 7. Plots of MgO versus oxides and compatible elements from the Kedanshan ultramafic-mafic intrusion.

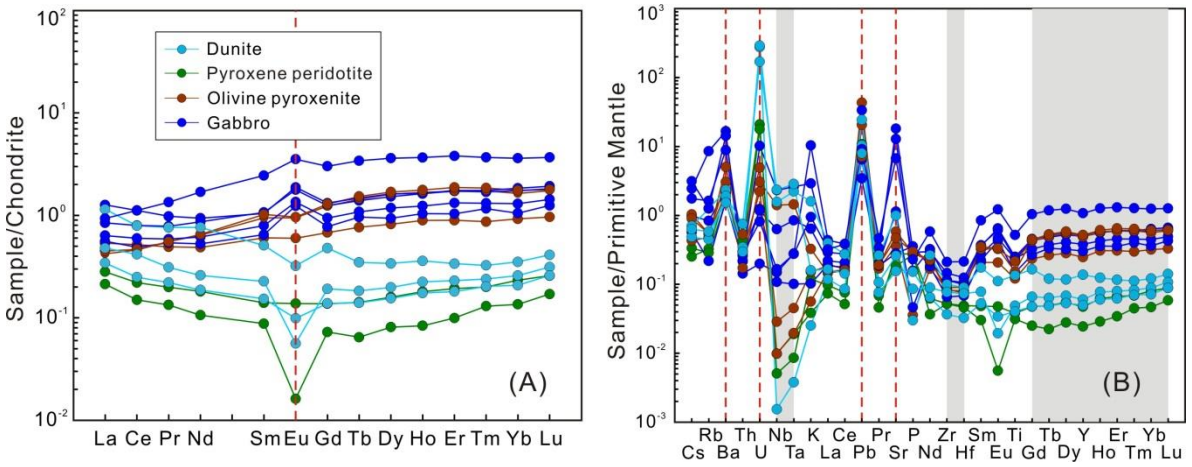

836

837 **Fig. 8.** Chondrite-normalized REE and primative mantle-nomalized multi-element patterns from the

838 Kedanshan ultramafic-mafic intrusion. Chondrite and primitive mantle normalizing values after Sun

839 and McDonough (1989).

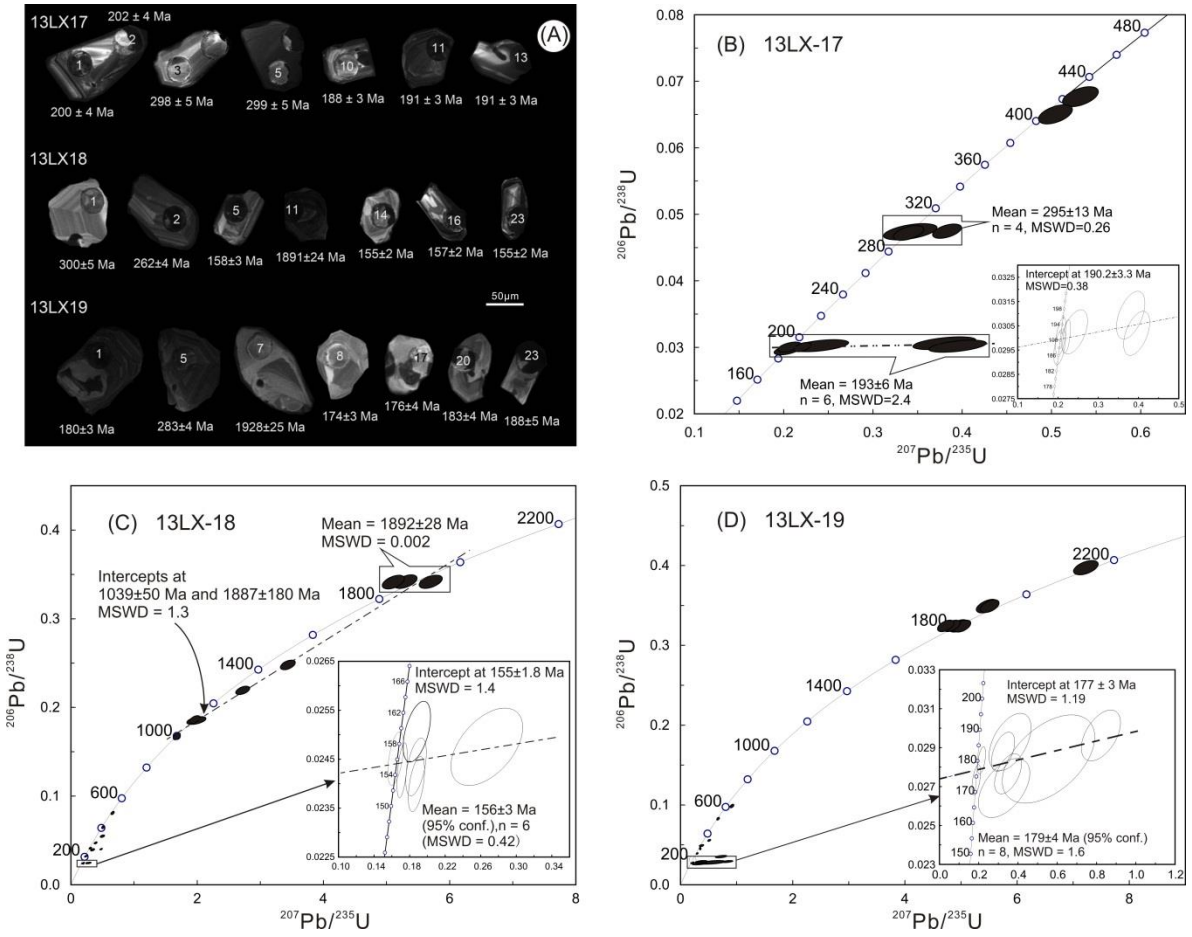

840

841 **Fig. 9.** CL images and concordia diagrams of zircon LA-ICP-MS analyses of gabbro samples from the

842 Kedanshan ultramafic-mafic intrusion.

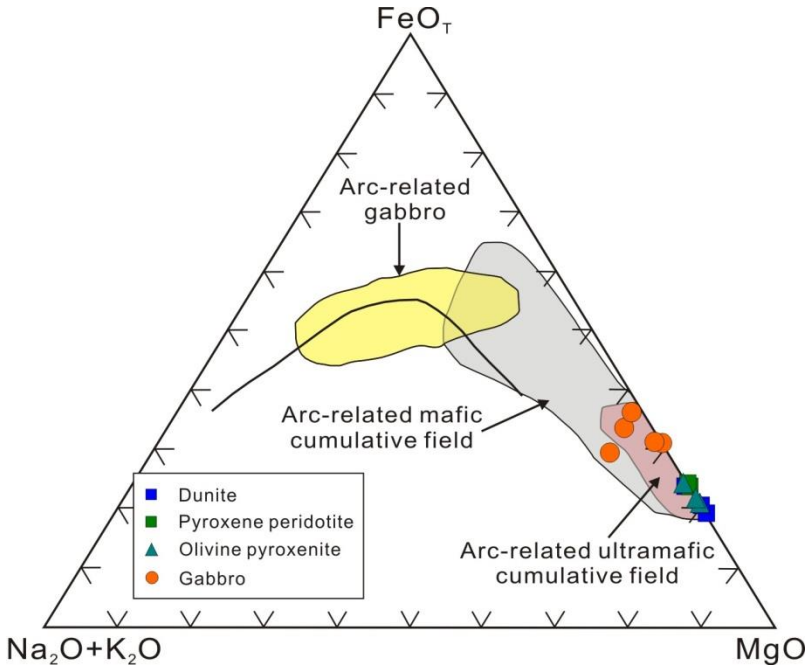

843

844 **Fig.10.** AFM diagram from the Kedanshan ultramafic-mafic intrusion (modified after Beard, 1986).

845

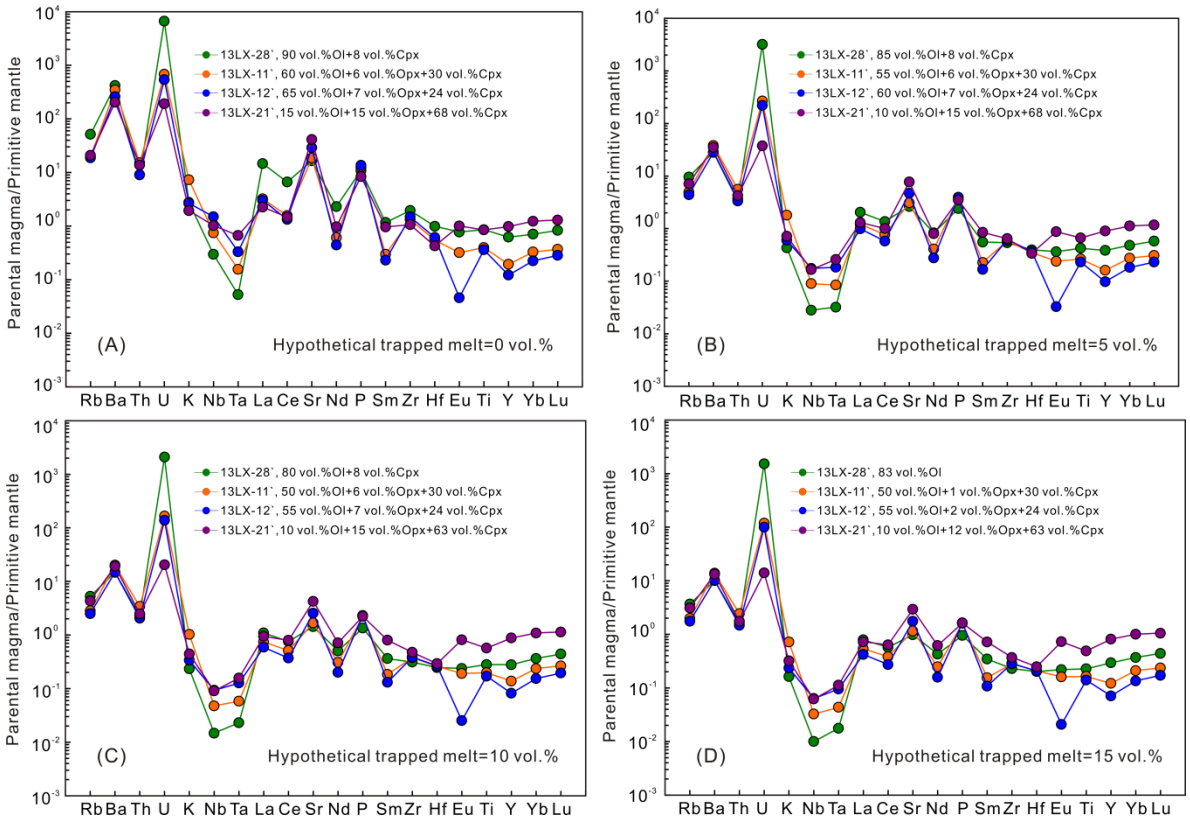

Fig.11 Primative mantle-nomalized multi-element patterns from the calculated parental magma compositions of the Kedanshan ultramafic-mafic intrusion. Normalization values of PM are from Sun and McDonough (1989).

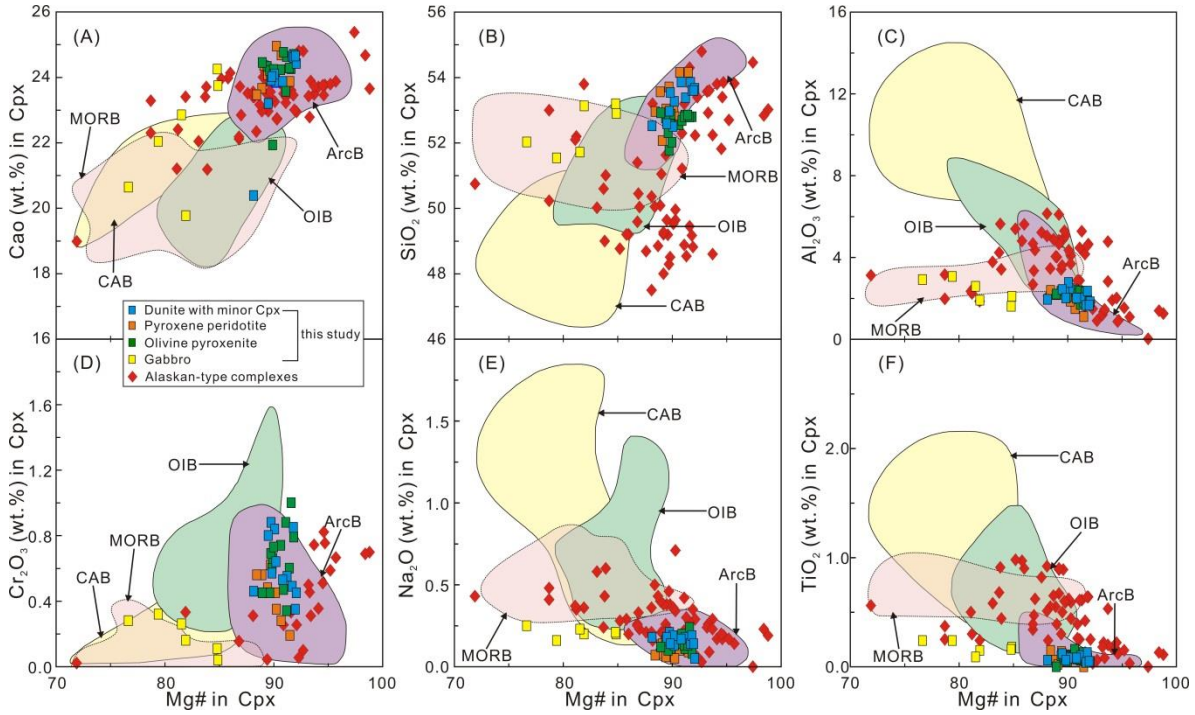

852

853 **Fig. 12.** Mg# versus major element contents in clinopyroxenes from the Kedanshan ultramafic-mafic

854 intrusion. Cpx composition fields from magmatic cumulate dunite, wehrlite, and clinopyroxenite

855 xenoliths hosted in arc basalts (ArcB), oceanic island basalts (OIB) and continental alkaline basalts

856 (CAB) after Kim and Choi (2016) and references therein; Cpx composition field from gabbros and

857 gabbroic rocks in MORB after Niu et al. (2002); Cpx compositions from Alaskan-type complexes

858 after Himmelberg and Loney (1995).

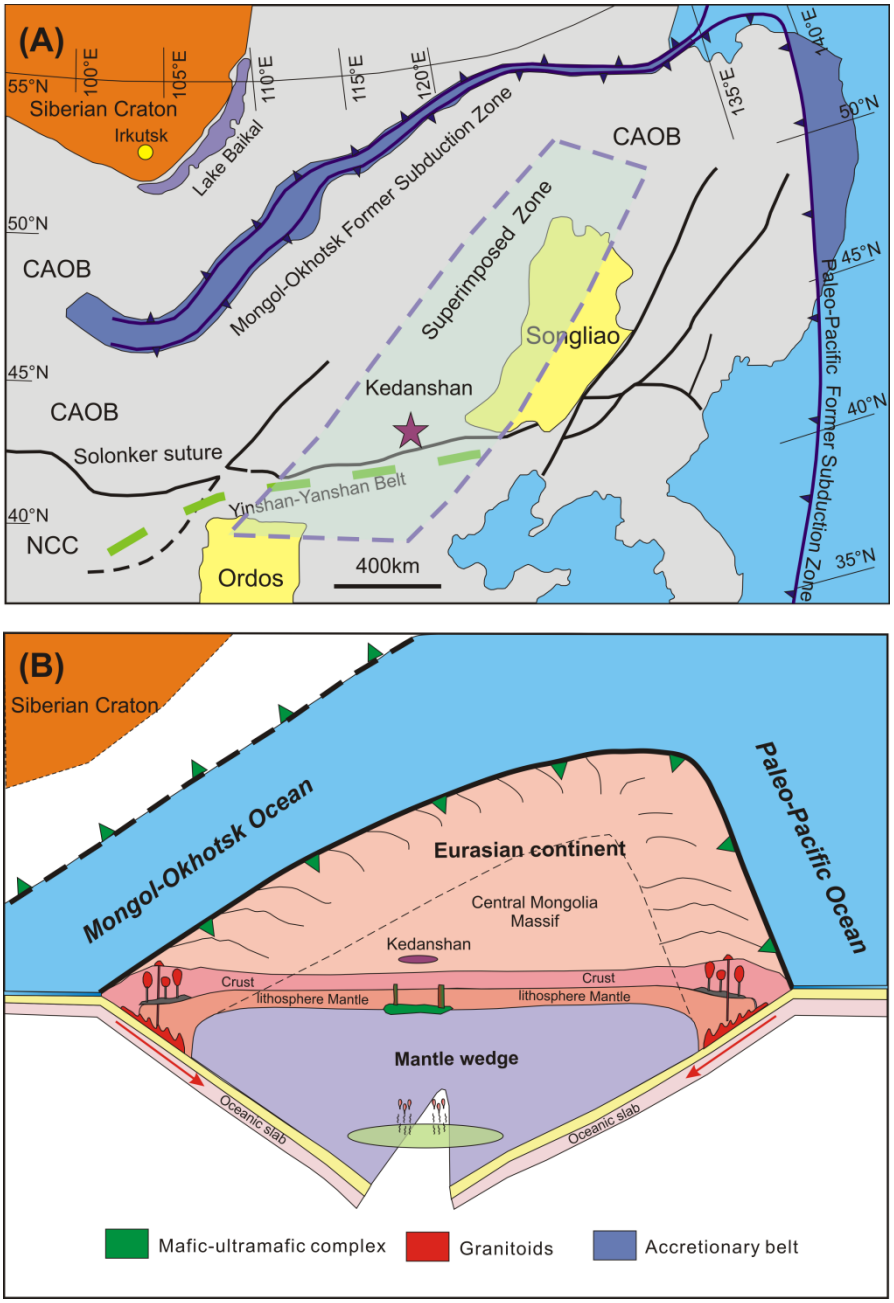

Fig. 13. A tectonic model showing a petrogenetic link between the Jurassic Kedanshan ultramafic-mafic intrusion and superimposed subduction. (A) A sketch map showing location of the Kedanshan ultramafic-mafic intrusion and former subduction zones of the Mongol-Okhotsk Ocean and Paleo-Pacific Ocean (modified after Wang et al., 2012). (B) A cartoon showing superimposed subduction of the Mongol-Okhotsk Ocean and Paleo-Pacific Ocean beneath the Central Mongolia Massif.